iScience

CellPress
OPEN ACCESS

Article

# Investigating the spatial interaction of immune cells in colon cancer

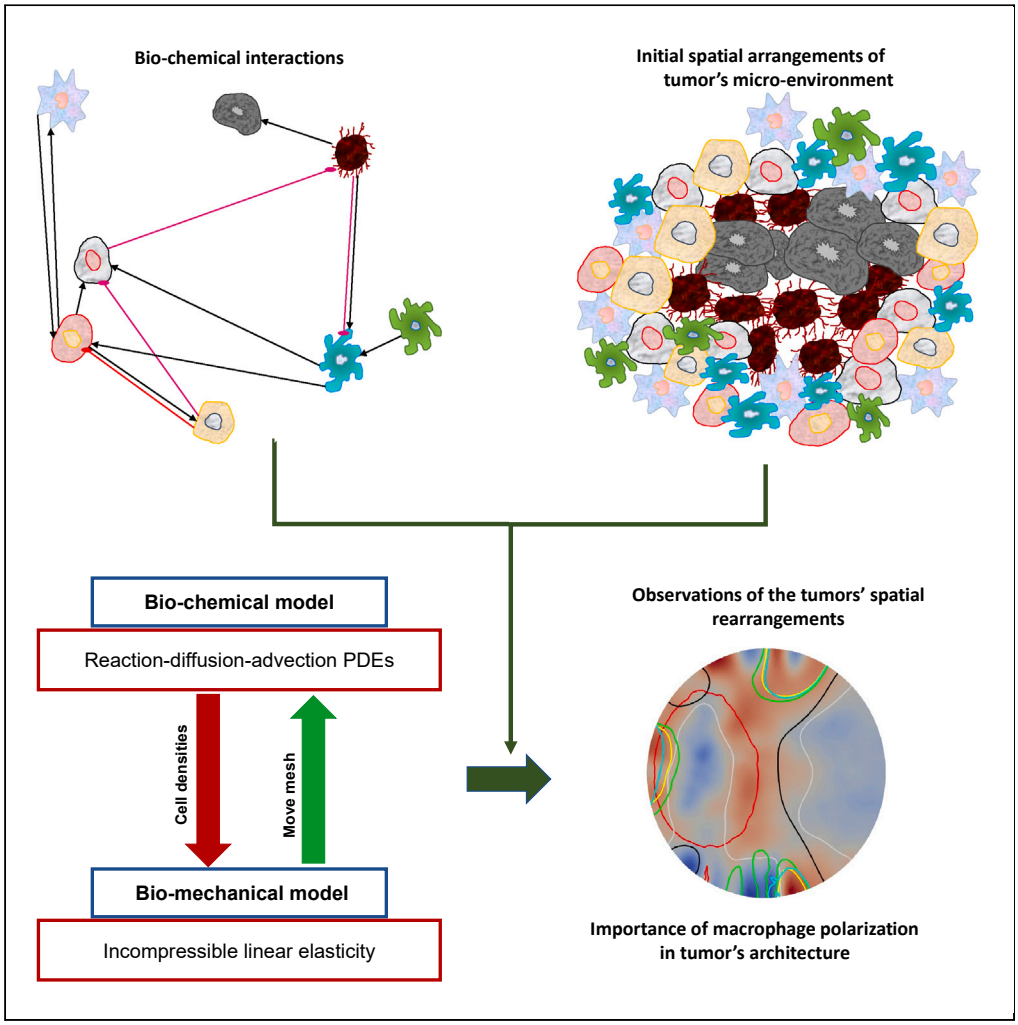


Navid Mohammad Mirzaei, Wenrui Hao, Leili Shahriyari

lshahriyari@umass.edu

## Highlights

Immune cell colocalizations control dynamics and patterns in the tumor microenvironment

Macrophages heavily affect the patterns in the colorectal tumor microenvironment

We use a biomechanical model to identify cells responsible for spatial arrangements

Macrophage polarization is crucial in arranging the colorectal tumor microenvironment

Mohammad Mirzaei et al., iScience 26, 106596
May 19, 2023 
https://doi.org/10.1016/j.isci.2023.106596

iScience

CellPress
OPEN ACCESS

Article

# Investigating the spatial interaction of immune cells in colon cancer

Navid Mohammad Mirzaei,[1] Wenrui Hao,[2] and Leili Shahriyari[1,3,*]

## SUMMARY

**The intricate network of interactions between cells and molecules in the tumor microenvironment creates a heterogeneous ecosystem. The proximity of the cells and molecules to their activators and inhibitors is essential in the progression of tumors. Here, we develop a system of partial differential equations coupled with linear elasticity to investigate the effects of spatial interactions on the tumor microenvironment. We observe interesting cell and cytokine distribution patterns, which are heavily affected by macrophages. We also see that cytotoxic T cells get recruited and suppressed at the site of macrophages. Moreover, we observe that anti-tumor macrophages reorganize the patterns in favor of a more spatially restricted cancer and necrotic core. Furthermore, the adjoint-based sensitivity analysis indicates that the most sensitive model's parameters are directly related to macrophages. The results emphasize the widely acknowledged effect of macrophages in controlling cancer cells population and spatially arranging cells in the tumor microenvironment.**

## INTRODUCTION

Colorectal cancer (CRC) is one of the most common types of cancer. In 2020, it accounted for 1.93 million cases and 916,000 deaths, placing it as the third most diagnosed and second most lethal cancer type worldwide.[1] Among all the diagnosed CRCs, about 71% are colon and 29% are rectum cancers.[2] Endoscopy, along with biopsy, is the main diagnostic procedure. Patients with CRC can be treated via direct surgical removal of the tumor, chemotherapy, radiotherapy, immunotherapy, and targeted drug therapy.[3–6] However, like all the other cancer types, there is still a possibility of recurrence after treatments, especially in the case of surgical removal of the tumor.[7,8] This makes non-surgical options more attractive, at least as a follow-up to the surgical removal procedure.[9] Unfortunately, factors like the diversity of gene profiles of cancer patients, their lifestyles and diet, and the complexity of the cancer microenvironment have made it impossible to come up with a single drug combination or target a certain cell type or pathway for everyone.

The tumor microenvironment (TME) is a region hosting cancer cells, infiltrating immune cells, necrotic cells, extracellular matrix, blood vessels, and secreted factors.[10] The numerous intricate interactions between cancer cells and other constituents of the microenvironment play a significant role in cancer progression. For example, the immune system, responsible for killing cancer cells, can have an opposite effect on cancer progression.[11,12] While some immune cells such as $CD8^+$ T cells show their expected cancer-inhibiting attribute either directly or through secretion of interferon (IFN)-$\gamma$ in many tumors, macrophages have a more controversial role.[13] Different Subtypes of tumor-associated macrophages (TAMs) (macrophages infiltrating the tumor microenvironment) can have completely opposite effects. For instance, the M1 macrophages can produce radicals that are deadly to tumors,[14,15] while M2 macrophages produce substances that promote cancer proliferation and invasion or impede $CD8^+$ T cells from reaching tumor cells.[16–19] Since macrophages are the most abundant leukocytes in the colon, such effects can have a decisive outcome.[20]

Moreover, the interactions between cells and cytokines in the microenvironment have motivated an ecological framework for cancer study that benefits from considering the spatial heterogeneity of the microenvironment.[21,22] For instance, one study confirms that the spatial distribution of TAMs is an important factor in predicting clinical outcomes.[23] Specifically, they show that lung tumors more proximal to M2-type macrophages have a higher chance of survival. Another study on ovarian cancer shows that the

[1]Department of Mathematics and Statistics, University of Massachusetts Amherst, Amherst, 01003 MA, USA

[2]Department of Mathematics, Pennsylvania State University, University Park, 16802 PA, USA

[3]Lead contact

*Correspondence: lshahriyari@umass.edu

https://doi.org/10.1016/j.isci.2023.106596

colocalization of $CD8^+$ T cells and B cells results in better prognoses.[24] It has also been shown that a prognosis based on the density and the location of immune cells works better than the classical histopathological methods for determining the stage of colorectal cancer.[25] On the other hand, the heterogeneity of the tumor microenvironment can lead to nonuniform drug delivery and, thus, inefficient therapy.[26] These are just a few examples of the importance of the tumor microenvironment and its spatial attributes in understanding and treating cancer.

Mathematical models can help scientists understand complex phenomena which are either impossible or costly to experiment with. The interaction network between cells and molecules in the tumor microenvironment can be modeled using a system of ordinary differential equations (ODEs).[27–33] One major benefit of these models is the simplicity of their simulation and parameter estimation. Kirshtein et al. propose a comprehensive data-driven ODE model of colon cancer microenvironment for five clusters of patients. They find out the inhibition of cancer by cytotoxic T cells, IFN-$\gamma$, and transforming growth factor $\beta$ (TGF-$\beta$) has the most significant effect on the population of cancer cells.[28] In addition, among all the immune cells, macrophages' activation and decay rates were the most sensitive parameters for 4 out of 5 clusters of patients. Mohammad Mirzaei et al. use the same approach for breast cancer using a PyMT-MMTV mouse model and realize that the promotion of cancer proliferation by adipocytes and interleukin-6 (IL-6) plays a significant role in the progression of breast tumors.[33] Dritschel et al. study the cytotoxic and helper T cell interactions with cancer cells in tumor microenvironment.[27] They show that depending on the T cell infiltration intensity, there are two bistability scenarios; one between cancer elimination and escape and the other between cancer escape and cancer coexistence with the immune cells. Despite valuable quantitative description and prediction of the dynamics of a system, ODE models fail to capture the spatial interactions and patterns that can significantly affect the system's overall behavior. This drawback motivates scientists to include spatial dependence in their models. This has been extensively pursued in modeling epidemiological and ecological phenomena, where the proximity of key role players can significantly affect their interaction and dynamics. The ODE models, however, provide a solid groundwork for building more realistic partial differential equation (PDE) models. These models can investigate the change of quantities in space and time. Given the importance of the spatial heterogeneity of the tumor microenvironment and its significance in cancer progression, treatment, and prognoses, PDE models can be a valuable extension to ODE models. Kim & Friedman investigate the early-stage progression of transformed epithelial cells through their interactions with the fibroblasts and extracellular matrix in the tumor microenvironment.[34] These interactions are formulated through the concentration of cytokines secreted by the mentioned cell types, such as epidermal growth factor (EGF), transforming growth factor (TGF-$\beta$), and matrix metalloproteinase (MMP). They make several hypotheses, one of which says that haptotaxis induces increased production of the tumor, cell migration, and MMP production. However, their model only considers one spatial dimension and neglects the effect of immune cell interactions in the tumor microenvironment. Mohammad Mirzaei et al. propose a PDE model of breast cancer progression based on PyMT-MMTV mouse data.[35] Their results show that, in the regions with more immune cells interaction, cancer population is less dense, and a constant influx of immune cells controls the tumor size and cancer population. But, they do not further investigate the patterns formed in the tumor microenvironment and the pathways responsible for them. On the other hand, Owen and Sherratt investigate the patterns and heterogeneity imposed on solid tumors by macrophages.[36] Their model includes the interaction between macrophages, tumor cells, and normal tissue cells. They investigate a traveling wave solution corresponding to the tumor progression through the normal cells, with spatial instability forming behind the wavefront. The tumor growth mechanisms in their model are minimalistic, and they do not consider the complex interactions in the tumor microenvironment.

In this paper, we extend and enhance an ODE model of colonic tumors introduced by Kirshtein et al.[28] to investigate the spatial interactions among key players in the tumor microenvironment. We develop a reaction-diffusion-advection (RDA) system of PDEs, with the ODE system accounting for the reaction terms. This model is equipped with a solid linear elasticity problem that governs the domain deformation. This is common assumption for solid tumors.[37–39] Since for small time steps, the change in strain and elastic response are proportional to each other,[40] this leads to a locally linear response. However, the advective effects dictated by biology introduce non-linear strains. Hence we assume that the domain deformation is related to changes in cell densities and is coupled with the system of PDEs through the advection term. To investigate the spatial effect of immune cells and their impact on cell dynamics, we model several extreme scenarios in which sources are installed within the tumor microenvironment, constantly injecting immune

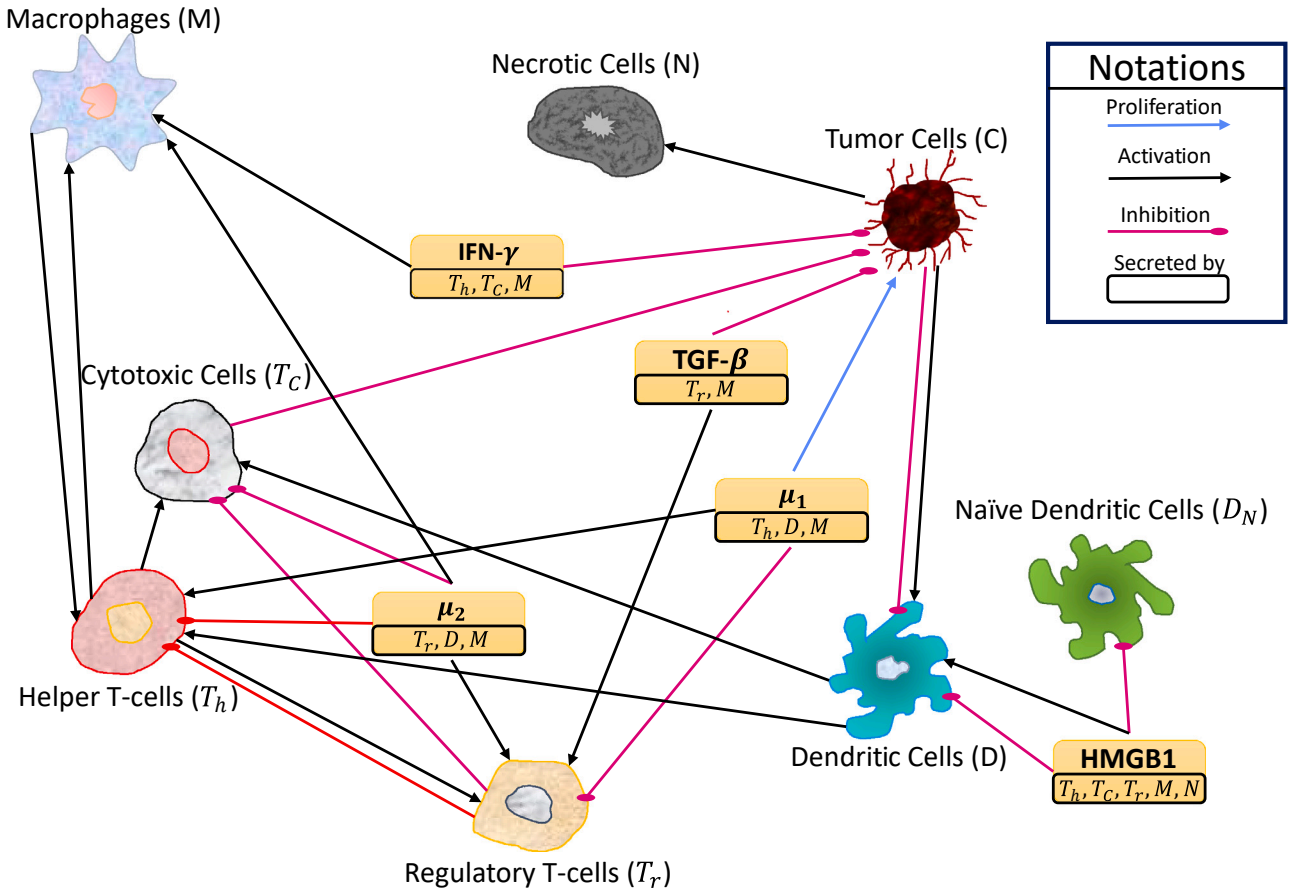


**Figure 1. Interaction network between cells and molecules in the tumor microenvironment**

The black arrows point from activators to the cell type they activate. The blunt red arrows point from inhibitors to the cell type they inhibit. The blue arrow implies that the cytokine group $\mu_1$ promotes tumor cell proliferation. Each cytokine group and the cell types they are secreted by are shown in the yellow boxes. Our model does not include different variables for macrophage subtypes. We do not include naive T cells in the tumor microenvironment interactions since they are mostly activated in the lymphoid system.

cells at separate locations. Finally, we perform several sensitivity analyses to investigate the importance of the parameters in our study. To the best of the authors' knowledge, there are not many (if any) studies that investigate the spatiotemporal patterns and their possible causes in the tumor microenvironment through an extensive reaction network and a free-boundary growth.

## RESULTS

We investigate the effect of the spatial interaction of immune cells and cancer on the dynamics of the tumor microenvironment in a controlled environment that is not necessarily replicable experimentally. The model is based on the interaction network of key players given in Figure 1 obtained by Kirshtein et al.[28] Table 1 shows the variable names and the corresponding data associated with each variable used in the model.

We create different scenarios where immune cells are injected into the environment constantly at separate locations; see Figure 2. We do not include naive T cells inside the tumor microenvironment (See STAR Methods section for more details).

The initial conditions for naive T cells, cancer, and necrotic cells and the reaction parameters $\boldsymbol{\theta}$ from Equation 20 are taken from the first cluster of patients in Kirshtein et al.[28] We assume the cancer population has a uniform distribution at the beginning and that necrotic cells do not exist initially. We also assume there are no molecules present at $t = 0$. The initial distributions of immune cells follow Figure 2.

**Table 1. State variables and their notations and definitions**

| Variable in PDE | Variable in ODE | Description |
|---|---|---|
| $[X_1]$ | $[T_N]$ | Naive T-cells |
| $[X_2]$ | $[T_h]$ | Helper T-cells |
| $[X_3]$ | $[T_C]$ | Cytotoxic T-cells and natural killer cells |
| $[X_4]$ | $[T_r]$ | Regulatory T-cells |
| $[X_5]$ | $[D_N]$ | Naive dendritic cells |
| $[X_6]$ | $[D]$ | Activated dendritic cells |
| $[X_7]$ | $[M]$ | Activated macrophages |
| $[X_8]$ | $[C]$ | Cancer cells |
| $[X_9]$ | $[N]$ | Necrotic cells |
| $[X_{10}]$ | $[H]$ | High mobility group box 1 (HMGB1) |
| $[X_{11}]$ | $[\mu_1]$ | IL-6, IL-17, IL-21, and IL-22 |
| $[X_{12}]$ | $[\mu_2]$ | IL-10 and Chemokine Ligand 20 (CCL20) |
| $[X_{13}]$ | $[I_\gamma]$ | IFN-$\gamma$ |
| $[X_{14}]$ | $[G_\beta]$ | TGF-$\beta$ |

The first column shows the variable notations in the PDE model, the second column shows their notation and definition in Kirshtein et al.,[28] and the last column shows their definition.

The results of the simulations show that an egg-shaped pattern appears at the right side of the region for some of the cells and most of the molecules after 3000 days (Figures 3 and 4). That region is significantly affected by macrophages, and given their involvement in the production of all the molecules; they seem to be the main reason for this behavior. Macrophages start close to their source location and accumulate more in an egg-shaped region. Regulatory T cells and naive dendritic cells have a significant presence at all the source locations. The other cell types and molecules, including cancer and necrotic cells, show the opposite behavior. Dendritic cells and helper T cells are highly colocalized since dendritic cells are an important activator of helper T cells. They both have a fairly significant presence everywhere in the domain and near their source location. Cytotoxic T cells quickly get recruited to the site of macrophages. It seems as if they mostly occupy a space that is the exact complement of where macrophages are focused. This is in line with the hindering effect of macrophages against $CD8^+$ cells mentioned in the introduction. In fact, all T cells seem to be avoiding that region, but the effect is much more visible for cytotoxic T cells. Cancer and necrotic cells are the most pronounced close to the tip and base of the egg-shaped region on the right side. They are also the least present at the immune cells' source locations. If we follow their progression, they accumulate around the macrophage source location and slowly spread to the rest of the domain.

Figure 5 better illustrates the spatial patterns and their relationship with cancer cells and the rest of the immune cells and cytokines. The contours super-imposed on cancer concentration mark the boundaries at which each cell type or molecule is precisely at its half concentration value. A quick look at Figures 3 and 4 can help to determine which side of each contour represents higher and which side represents lower concentrations of their respective quantity. Importantly, there are two general patterns shown in Figures 3, 4, and 5: (1) the circular regions formed at the immune cells' source locations and (2) the egg-shaped regions formed around the macrophage source at the right side. Below, we discuss these patterns in detail.

- We see circular regions for all cells and cytokines at the source locations. We speculate that some pathway induced by regulatory T cells ($T_r$) might be the main reasons for forming the circular patterns for most cells and cytokines. Regulatory T cells inhibit other T cells, and together they are involved in activating macrophages and secreting all the cytokines. But what about the dendritic, cancer, and necrotic cells? For naive dendritic cells ($D_N$), our reaction network in Figure 1 shows that they are only inhibited by *HMGB1*.[44] That is why their pattern looks like it complements the *HMGB1* pattern. So $T_h$ indirectly affects $D_N$ too since all T cells are involved in producing *HMGB1*. In addition, activated dendritic cells $D$ differentiate from $D_N$, so their pattern is also complementary at the circular regions. Regarding the reactions in the model, none of the mentioned cell types except for cytotoxic T cells ($T_C$) directly inhibit or promote cancer proliferation. But the cytotoxic T cells do not have a significant presence in the circular regions. Similarly, none of the inhibiting

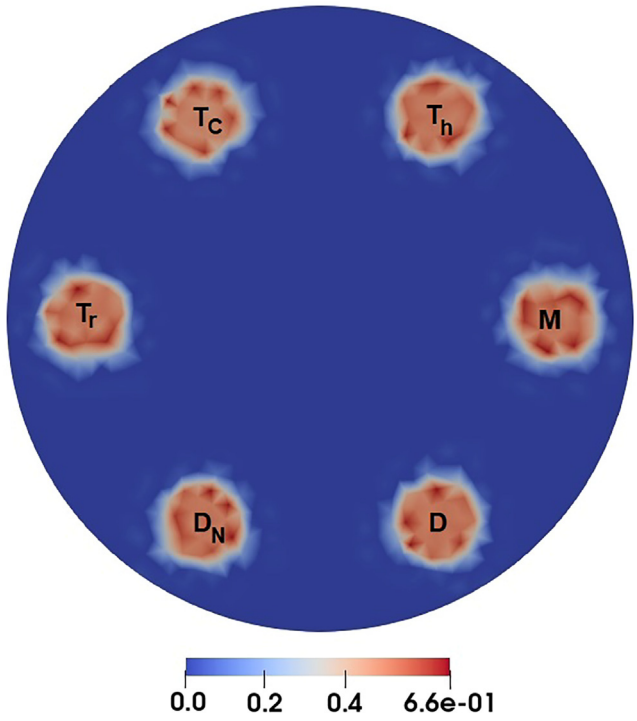


**Figure 2. Location of each immune cell source inside the tumor microenvironment**

The value shown by the color bar is non-dimensional. The rest of the variables are not shown because cancer cells have a uniform distribution at the beginning, and cytokines start from zero initial value.

cytokines like IFN-$\gamma$ and TGF-$\beta$ have a strong presence in these circular regions. This leaves us with two possible justifications: (1) cancer-promoting cytokines group $\mu_1$, which is secreted by dendritic cells, macrophages, and helper T cells, has such a significant effect that its lack of expression at those locations leaves a considerable impact on cancer distribution and (2) the total effect of the reactions in the model is creating a velocity field that repels the cancer cells and possibly other cells with the same pattern from those locations. Figure 6 can attest to the second justification.

- We see an egg-shaped pattern located at the right side of the region. This region is heavily populated by macrophages, given the proximity of their source location. Unlike the other cell types, macrophages do not seem to wander off to other places in the domain. This suggests that they are the main reason for this egg-shaped pattern. Since macrophages are involved in producing all the cytokines, they have more or less affected all the cytokines' patterns. Helper T cells and activated dendritic cells are more pronounced close to the macrophage's source since they are activated by cytokines group $\mu_1$ and *HMGB*1, respectively. Cytotoxic T cells quickly get recruited to the site of macrophages' location. This is due to their activators $T_h$ and $D$, which have a significant presence close to that region. In fact, helper T cells and dendritic cells play an essential role in activating cytotoxic T cells by producing priming chemokines and cross-presenting exogenous antigens, respectively.[45,46] Additionally, regulatory T cells, which act as $T_C$ inhibitors, have much lower levels there due to being inhibited by $\mu_1$. Now, the reason that the number of cancer cells is higher closer to the egg-shaped region is not clear from these results. We mentioned that the pro-tumor cytokines group $\mu_1$ is more pronounced inside the egg-shaped region. Other cells and cytokines with mixed and indirect effects, such as macrophages, dendritic cells, *HMGB*1, and $\mu_2$, are also abundant in this region. However, one can deduce that pro-tumor activity dominates the anti-tumor activity for this behavior. Since $\mu_1$ is the only pro-tumor pathway in the model, the pro-tumor attributes of $\mu_1$ can be the main cause, or there might be a more complex underlying interplay involved. For instance, the macrophages act more as pro-tumors rather than anti-tumors. Note, the observed egg shape of the region has no significance as it is an artifact of the geometry and the segregated immune cell locations. These results only indicate that the macrophage patterns dictate the

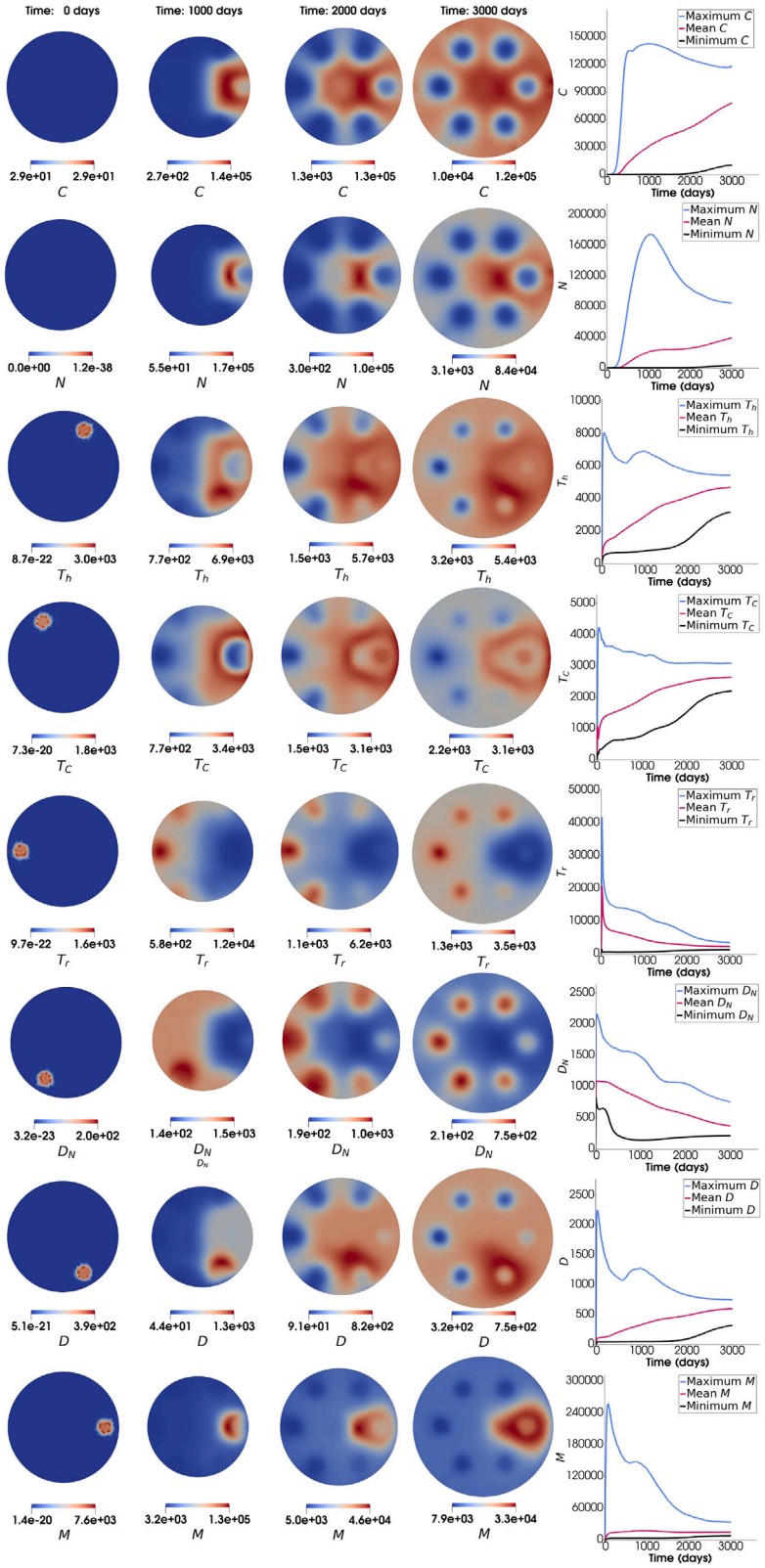
Time: 0 days
Time: 1000 days
Time: 2000 days
Time: 3000 days
2.9e+01 2.9e+01 C
2.7e+02 1.4e+05 C
1.3e+03 1.3e+05 C
1.0e+04 1.2e+05 C
Maximum C
Mean C
Minimum C
C
Time (days)
0.0e+00 1.2e-38 N
5.5e+01 1.7e+05 N
3.0e+02 1.0e+05 N
3.1e+03 8.4e+04 N
Maximum N
Mean N
Minimum N
N
Time (days)
8.7e-22 3.0e+03 $T_h$
7.7e+02 6.9e+03 $T_h$
1.5e+03 5.7e+03 $T_h$
3.2e+03 5.4e+03 $T_h$
Maximum $T_h$
Mean $T_h$
Minimum $T_h$
$T_h$
Time (days)
7.3e-20 1.8e+03 $T_C$
7.7e+02 3.4e+03 $T_C$
1.5e+03 3.1e+03 $T_C$
2.2e+03 3.1e+03 $T_C$
Maximum $T_C$
Mean $T_C$
Minimum $T_C$
$T_C$
Time (days)
9.7e-22 1.6e+03 $T_r$
5.8e+02 1.2e+04 $T_r$
1.1e+03 6.2e+03 $T_r$
1.3e+03 3.5e+03 $T_r$
Maximum $T_r$
Mean $T_r$
Minimum $T_r$
$T_r$
Time (days)
3.2e-23 2.0e+02 $D_N$
1.4e+02 1.5e+03 $D_N$
1.9e+02 1.0e+03 $D_N$
2.1e+02 7.5e+02 $D_N$
Maximum $D_N$
Mean $D_N$
Minimum $D_N$
$D_N$
Time (days)
5.1e-21 3.9e+02 D
4.4e+01 1.3e+03 D
9.1e+01 8.2e+02 D
3.2e+02 7.5e+02 D
Maximum D
Mean D
Minimum D
D
Time (days)
1.4e-20 7.6e+03 M
3.2e+03 1.3e+05 M
5.0e+03 4.6e+04 M
7.9e+03 3.3e+04 M
Maximum M
Mean M
Minimum M
M
Time (days)

**Figure 3. Spatial and temporal evolution of the model cell types**

Parameters are extracted from Kirshtein et al.[28] and Table 2. The first four columns show the spatial distribution of each cell type at times $t = 0, 1000, 2000$ and 3000. The maximum, mean, and minimum curves in the fifth column correspond to $\max_{\mathbf{x}\in\Omega(t)}[X_i](\mathbf{x},t)$, $\text{mean}_{\mathbf{x}\in\Omega(t)}[X_i](\mathbf{x},t)$, $\min_{\mathbf{x}\in\Omega(t)}[X_i](\mathbf{x},t)$, respectively, for the associated cell type $[X_i]$ and the domain at time $t$ (i.e., $\Omega(t)$). There is an egg-shaped region close to the macrophage source location, which seems to impact several other cells like cancer, necrotic, and T cells. Cancer and necrotic cells obtain their highest value close to the tip of this egg-shaped region. Helper T cells show high colocalization with dendritic cells close to the dendritic cells' source location.

microenvironment arrangement and have important implications for the spatial heterogeneity of the tumor microenvironment.

Note that, to avoid complexity, a fraction of cancer cell death is the model's only source of necrotic cell production. As a result, their behavior is similar to cancer cells. However, we noticed two interesting spatial patterns for cancer and consequentially necrotic cells: (1) the circular patterns at the immune cells source locations where cancer and necrotic cells are the least present and (2) the egg-shaped region at the right side of the domain where they are both more abundant. The former is probably due to the shortage of promoting factors such as $\mu_1$ or the direction of the velocity field at those locations since there are no other inhibiting factors in those regions. The latter is more obscure since many types of anti- and pro-tumor factors are present in that area. In other words, it is not clear which effect is more dominant, the effect of pro-tumor factors or the effect of anti-tumor factors. But it is certainly interesting to observe that, in our simulations, cytotoxic T cells travel quickly and purposefully to the site of macrophages and get blocked by them. The way the spatial distribution of $T_C$ and $M$ complement each other throughout the simulation is noteworthy. Furthermore, most of the cytokines follow the same pattern as macrophages. This suggests that macrophages play an essential role in arranging the microenvironment. Although the sensitivity analysis in Kirshtein et al.[28] suggests that the cancer population is sensitive to the parameters involved in the macrophage ODE, still, they come secondary to the parameters involved in the ODE governing cancer. Therefore, standard ODE models can easily overlook spatial effects like our observation.

The observed spatial effects discussed above are not particular to the specific experiment we designed initially. We further confirmed our results by investigating three cases with a random distribution of immune cell sources. We also considered random geometries to see whether our results were sensitive to the shape of the tumor microenvironment or not. Figures S1–S3 show our results. Due to the mechanical boundary condition, which is a function of the curvature Equation 30, the domains change according to the curvature flow and converge to almost a circular region. Just like in the controlled case, the spatial effect of macrophages can be traced in the rest of the cells and cytokines. All three figures show that cytotoxic T cells are suppressed in regions with high macrophage presence, and cancer cells are more abundant. We can also see regions of high colocalization between helper T cells and dendritic cells, similar to the controlled case.

To investigate further, we create two extreme cases. One by entirely blocking the $\mu_1$ production by macrophages and making them anti-tumors and another by blocking IFN-$\gamma$ and TGF-$\beta$ production by macrophages and making them pro-tumor. The results indicate many pattern changes (Figure 7; to avoid cluttering, we refrained from showing the other time steps and the evolution of minimum, mean, and maximum values).

**Table 2. Diffusion coefficients for the state variables used in the PDE system**

| i | $D_i$ value | Unit | Reason |
|---|---|---|---|
| 1 | 0 | $\frac{cm^2}{day}$ | Naive T-cells are not a part of the microenvironment |
| 2,3,4,5,6,8,9 | $8.64 \times 10^{-6}$ | $\frac{cm^2}{day}$ | Liao et al.[41] |
| 10 | $7.9 \times 10^{-2}$ | $\frac{cm^2}{day}$ | Hao and Friedman[42] |
| 11,12,13,14 | $1.25 \times 10^{-3}$ | $\frac{cm^2}{day}$ | Liao et al.[43] |

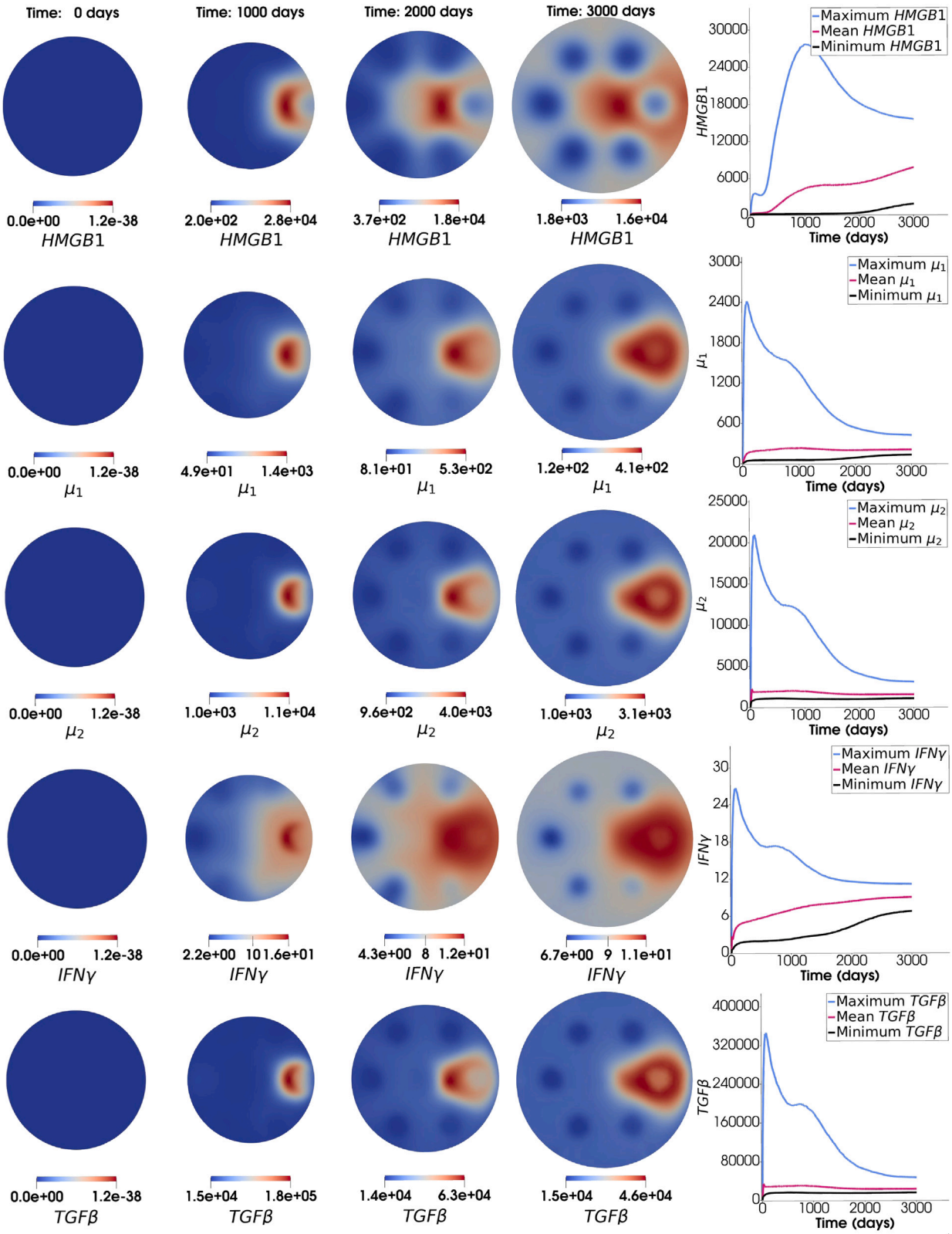
Time: 0 days
Time: 1000 days
Time: 2000 days
Time: 3000 days
0.0e+00 1.2e-38 HMGB1
2.0e+02 2.8e+04 HMGB1
3.7e+02 1.8e+04 HMGB1
1.8e+03 1.6e+04 HMGB1
Maximum HMGB1
Mean HMGB1
Minimum HMGB1
HMGB1
Time (days)
0.0e+00 1.2e-38 μ1
4.9e+01 1.4e+03 μ1
8.1e+01 5.3e+02 μ1
1.2e+02 4.1e+02 μ1
Maximum μ1
Mean μ1
Minimum μ1
μ1
Time (days)
0.0e+00 1.2e-38 μ2
1.0e+03 1.1e+04 μ2
9.6e+02 4.0e+03 μ2
1.0e+03 3.1e+03 μ2
Maximum μ2
Mean μ2
Minimum μ2
μ2
Time (days)
0.0e+00 1.2e-38 IFNγ
2.2e+00 10 1.6e+01 IFNγ
4.3e+00 8 1.2e+01 IFNγ
6.7e+00 9 1.1e+01 IFNγ
Maximum IFNγ
Mean IFNγ
Minimum IFNγ
IFNγ
Time (days)
0.0e+00 1.2e-38 TGFβ
1.5e+04 1.8e+05 TGFβ
1.4e+04 6.3e+04 TGFβ
1.5e+04 4.6e+04 TGFβ
Maximum TGFβ
Mean TGFβ
Minimum TGFβ
TGFβ
Time (days)

**Figure 4. Spatial and temporal evolution of the model molecules**

Parameters are extracted from Kirshtein et al.[28] and Table 2. The first four columns show the spatial distribution of each cytokine at times $t = 0, 1000, 2000$ and 3000. The maximum, mean, and minimum curves in the fifth column correspond to $\max_{\mathbf{x}\in\Omega(t)}[X_i](\mathbf{x},t)$, $\text{mean}_{\mathbf{x}\in\Omega(t)}[X_i](\mathbf{x},t)$, $\min_{\mathbf{x}\in\Omega(t)}[X_i](\mathbf{x},t)$ in ng/L, respectively, for the associated cytokine $[X_i]$ and the domain at time $t$ (i.e., $\Omega(t)$). All cytokines are affected by the macrophage-mediated egg-shaped region seen in Figure 3.

In terms of interactions, the cytokine group directly promotes cancer proliferation (see Figure 1). Therefore, blocking $\mu_1$ production by macrophages significantly reduces the overall production of $\mu_1$ in the TME and negatively impacts the cancer population. Even though macrophages do not change their spatial pattern, preventing them from producing the pro-tumor cytokines $\mu_1$ causes a significant change in the microenvironment patterns. Cancer and necrotic cells are now more focused in the center. Helper T cells are now more inclined toward the left, unlike in the first case. More importantly, it changes the cytotoxic regions by focusing the $T_C$ cells toward the left and center of the region. In this case, cytotoxic T cells are no longer being suppressed by macrophages and are strongly present where cancer cells are located. As a result, the final population of cancer cells is much less in this case than in the first results. Moreover, regulatory T cells also change their pattern, focusing more on the right and top-right of the domain. Naive dendritic cells are still located around the source locations, but they are much more intense now, and active dendritic cells show a significant migration to the center part of the tumor. Among the cytokines, $\mu_2$ and TGF-$\beta$ maintain their original pattern more or less. But $\mu_1$ no longer is egg shaped, which is expected since it is not produced by macrophages anymore. HMGB1 is now mainly in the center, and IFN-$\gamma$ is less egg shaped and more dragged toward the center. For the pro-tumor case, looking at the reaction network in Figure 1, we can see that IFN-$\gamma$ and TGF-$\beta$ directly inhibit cancer proliferation. Therefore, reducing their levels by blocking their production via macrophages should lead to a lower cancer population. Additionally, decreasing IFN-$\gamma$ and TGF-$\beta$ results in decreased levels of macrophages and regulatory T cells, which causes less helper T cell differentiation and, consequently, less cytotoxic T cell numbers in the TME. So, reduced levels of IFN-$\gamma$ and TGF-$\beta$ have direct and indirect pro-tumor effects. In terms of the spatial distributions, regardless of the changes in the final values, the patterns look pretty similar to the original case. For IFN-$\gamma$ and TGF-$\beta$, they follow the pattern of their other sources. In other words, IFN-$\gamma$ is now affected by $T_h$ and $T_C$ patterns and TGF-$\beta$ by $T_r$. Maybe the most important visible change in cells' distribution is the distribution of cancer cells. An egg-shaped pattern is more discernible now, meaning macrophages have been more successful in preventing the anti-tumor responses, especially from $T_C$ cells.

To share the results of our sensitivity analysis, it is best to get acquainted with our parameter-naming schemes. Besides the diffusion parameters we introduced earlier, we have six other sets of parameters; see Table 3.

We find the sensitivity of 4 objective functions to the parameters of our problem using adjoint-based sensitivity analysis (see the STAR Methods section for more detail). The objective functions are as follows:

$$J_1 = \int_0^T \int_{\Omega(t)} C(\mathbf{x},t)\, d\mathbf{x}\, dt, \qquad \text{(Equation 1)}$$

$$J_2 = \int_0^T \int_{\Omega(t)} \frac{C(\mathbf{x},t)}{T_h(\mathbf{x},t)+T_C(\mathbf{x},t)+T_r(\mathbf{x},t)+D_N(\mathbf{x},t)+D(\mathbf{x},t)+M(\mathbf{x},t)}\, d\mathbf{x}\, dt, \qquad \text{(Equation 2)}$$

$$J_3 = \int_0^T \int_{\Omega(t)} \|\mathbf{v}(\mathbf{x},\mathbf{t})\|\, d\mathbf{x}\, dt, \qquad \text{(Equation 3)}$$

$$J_4 = \int_0^T \int_{\Omega(t)} \omega(\mathbf{x},t)\, d\mathbf{x}\, dt, \qquad \text{(Equation 4)}$$

where $\omega(\mathbf{x},t)$ is the angle that the position vector of each mesh point makes with the positive $x$-axis. We picked these four objective functions because the total cancer population and cancer-immune cells ratio have important prognostic values. Also, the norm of the velocity field and $\omega(\mathbf{x},t)$ can be a good measurement of the microenvironment spatial arrangement. The functional $J_3$ quantifies the total speed of cell movements in the domain, and $J_4$ gives a scalar quantification of the collective direction of the movement. The parameters which are subject to our sensitivity analysis of functions Equations 1, 2, 3, and 4 include the reaction parameters introduced in Table 3 and diffusion coefficients. We do not include the location of

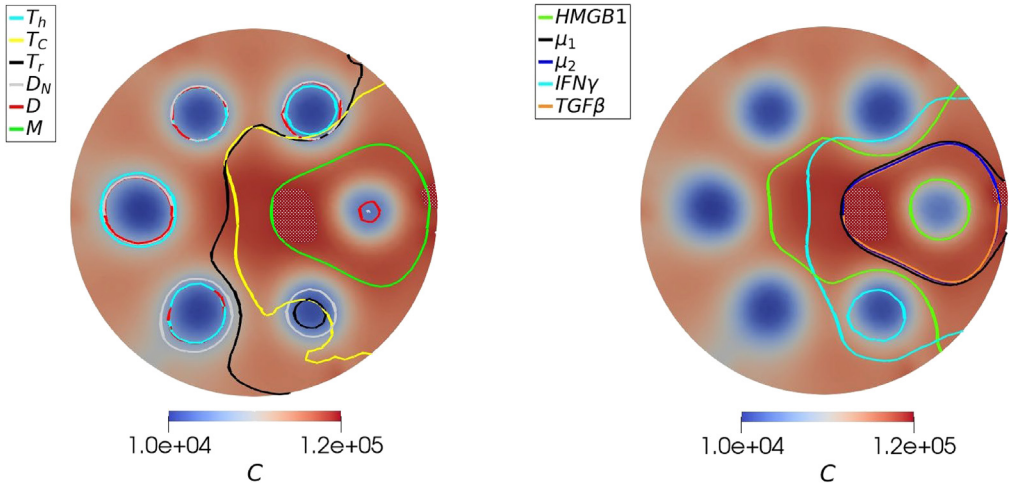


**Figure 5. Cells and molecules half-concentration contours**

The contours are super-imposed on cancer distribution for $t$ = 3000 days. The patterned regions show locations where cancer concentration is higher than 95% of its maximum value. Two patterns are evident in both figures. The egg-shaped region and the circular regions coincide with the immune cells source locations.

sources (i.e., $(A_i, B_i)$ in Equation 21) as parameters for sensitivity analysis for two reasons: (1) the location of the sources is based on a possibly unrealistic experiment assumption, as mentioned before, and it is trivial that moving them around will change the microenvironment arrangement and (2) their addition to the sensitivity problem as parameters jeopardizes the bilinearity of the weak form Equation 42, which is undesirable. Instead, in the appendix, we have included results based on randomly generated sources and boundary geometry. Figure 8 shows the top 20 most sensitive parameters for each of the objective functions Equations 1, 2, 3, and 4. Negative values mean that, if we increase the value of that parameter, it decreases the value of its corresponding objective function and vice versa.

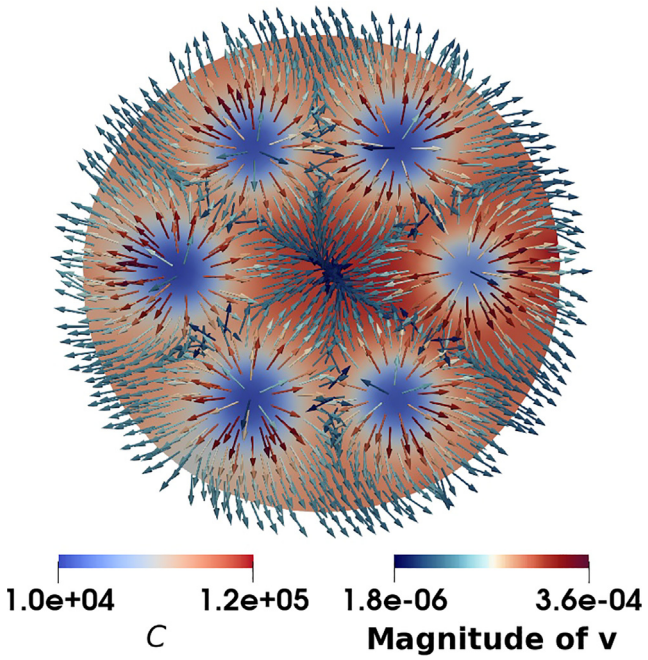


**Figure 6. Cells velocity field**

The velocity field is super-imposed on cancer distribution for $t$ = 3000 days. The arrows show the velocity field of the microenvironment. The color bar indicates the magnitude of the velocity field (speed) at each point.

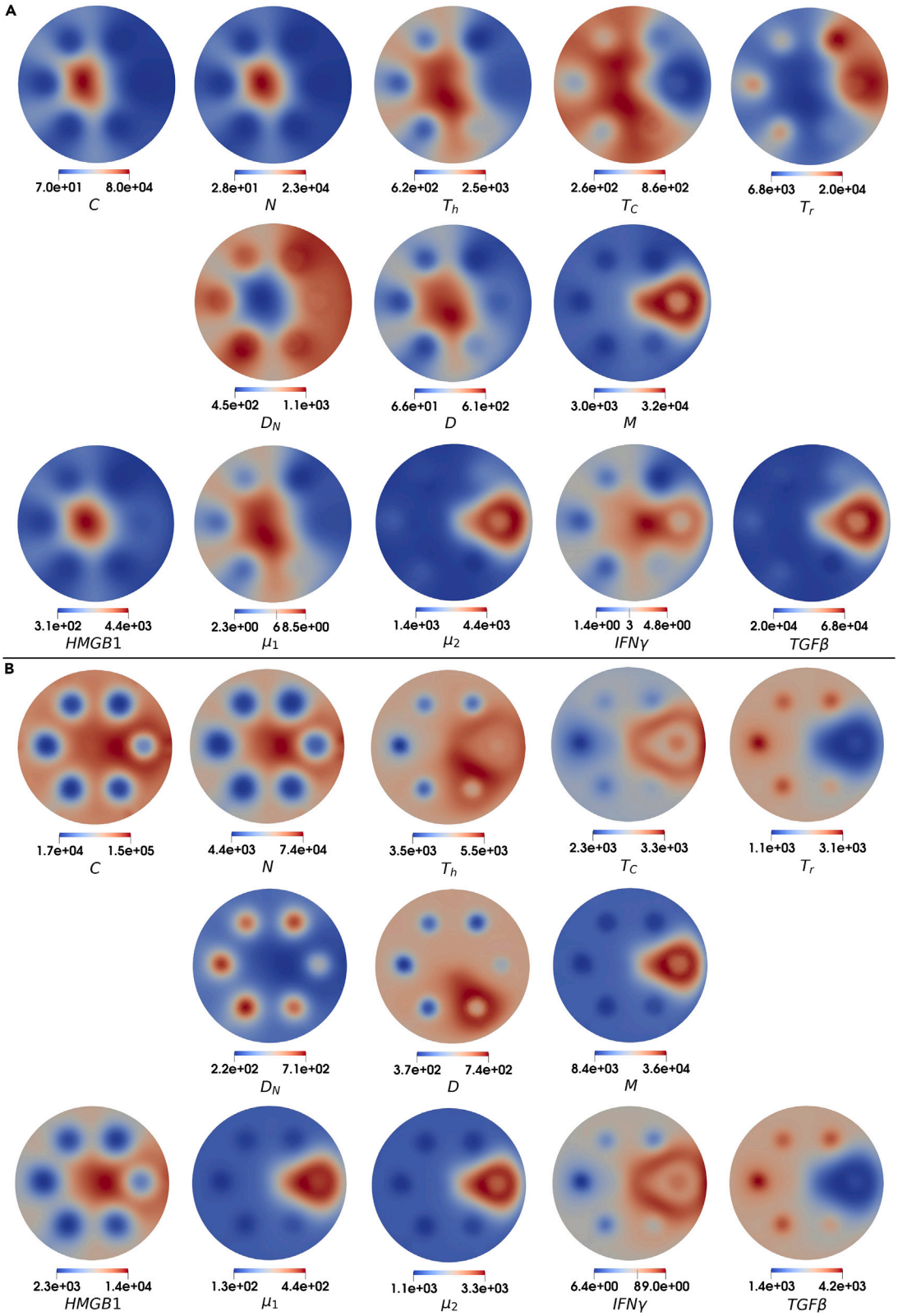
A
7.0e+01 8.0e+04
C
2.8e+01 2.3e+04
N
6.2e+02 2.5e+03
$T_h$
2.6e+02 8.6e+02
$T_C$
6.8e+03 2.0e+04
$T_r$
4.5e+02 1.1e+03
$D_N$
6.6e+01 6.1e+02
D
3.0e+03 3.2e+04
M
3.1e+02 4.4e+03
HMGB1
2.3e+00 6 8.5e+00
$\mu_1$
1.4e+03 4.4e+03
$\mu_2$
1.4e+00 3 4.8e+00
IFNγ
2.0e+04 6.8e+04
TGFβ
B
1.7e+04 1.5e+05
C
4.4e+03 7.4e+04
N
3.5e+03 5.5e+03
$T_h$
2.3e+03 3.3e+03
$T_C$
1.1e+03 3.1e+03
$T_r$
2.2e+02 7.1e+02
$D_N$
3.7e+02 7.4e+02
D
8.4e+03 3.6e+04
M
2.3e+03 1.4e+04
HMGB1
1.3e+02 4.4e+02
$\mu_1$
1.1e+03 3.3e+03
$\mu_2$
6.4e+00 89.0e+00
IFNγ
1.4e+03 4.2e+03
TGFβ

**Figure 7. Effect of macrophage subtypes on cells and cytokines distribution**

The figures show the distributions after $t$ = 3000 days with (A) Anti-tumor macrophages (blocked $\mu_1$ production) keep their egg-shaped pattern, but helper T cells, dendritic, cancer, and necrotic cells are now more focused in the center. Regulatory and cytotoxic T cells show opposing patterns, with cytotoxic cells no longer being suppressed by macrophages in the high-concentration cancer regions. The distribution of cytokines is mainly affected by macrophages except for $\mu_1$ and HMGB1.

(B) Pro-tumor macrophages (blocked IFN-$\gamma$ and TGF-$\beta$ production) keep their egg-shaped pattern; the rest of the cell patterns are similar to Figure 3. Cancer and necrotic cells are more pronounced in the egg-shaped region in this scenario. The two blocked cytokines IFN-$\gamma$ and TGF-$\beta$ follow the pattern of their other sources, i.e., $T_h$, $T_C$ for IFN-$\gamma$ and $T_r$ for TGF-$\beta$.

The sensitive reaction parameters agree with the findings of the ODE study.[28] However, in that study, for each patient cluster, when the sensitivity of cancer to parameters $\lambda_{M\mu_2}$, $\lambda_{MI_\gamma}$, and $\lambda_{MT_h}$ is negative, we get a positive value for $\delta_M$ and vice versa. However, here, all of them attain negative values. We validated the signs by running several experiments on these parameters and comparing the total cancer values. The difference between patients comes from the difference in their immune profiles. More specifically, the patients with positive sensitivity for the activation rates and negative for $\delta_M$ started with much lower total macrophages than the ones with the opposite behavior. This can be simply due to some parts of the domain acting like one patient and others acting like another, which constantly changes as the macrophages, other cells, and cytokines move around. This can be an interesting instance of the difference between ODE and PDE models. Furthermore, as expected, the cancer production and inhibition parameters are largely effective at controlling the cancer population and cancer-immune cell ratio. However, they are not the most sensitive parameters. The diffusion coefficients are the top parameters for each objective function. Given the spatial nature of these coefficients, it is expected to see them among the most sensitive parameters for spatial measures such as $J_3$ and $J_4$. As for $J_1$ and $J_2$, increasing the diffusion increases the cell-cell or cell-cytokine handshakes. For example, increasing cancer diffusion exposes them to more anti-tumor agents. Therefore, it kills more of them, or the diffusion of macrophages leads to less localized IFN-$\gamma$ and TGF-$\beta$ distributions, which inhibit cancer. However, these parameters are obscure. For instance, the motion of cells can differ based on the cellular matrix properties, effects such as chemotaxis or durotaxis, etc. So, it is hard to directly relate them to a certain biological factor in our model that can be controlled experimentally. Aside from that, we should point out the importance of macrophage-related parameters in all four sensitivity results. This is in line with our initial results about macrophages' overwhelming involvement in tumor microenvironment dynamics and arrangement.

All four objective functions are sensitive to the parameters inside red boxes, which means they control cancer and cancer-immune cell ratio and spatial measures such as the magnitude and orientation of the cell movements. We perturb the parameters in red boxes to see their effect on the objective values. We do a 75% perturbation to get more discernible changes. To clarify, whenever we use the term perturbation in this study, we refer to a random deviation with a certain magnitude from a known numerical value. The results show that the overall population of cancer changes significantly (Figure 9). The pattern of regions with the highest cancer population also undergoes a drastic change. It moves from the center to near the boundary at the right side. Other cells and cytokines also change their pattern, some slightly and some very extremely. For instance, the circular contours for $T_h$, $D_N$, and $D$ slightly change their diameters. On the other hand, we see drastic changes in the contours for $T_r$ and $T_C$. Additionally, the size of the egg-shaped contour changes for $M$, and its area shrinks from left to right. As for the cytokines, we see a significant change in the contours pattern for *HMGB*1 and IFN-$\gamma$. For $\mu_1$, $\mu_2$, and TGF-$\beta$, we see a slight change in the area enclosed by the egg-shaped contours. Perturbing the common sensitive parameters

**Table 3. Naming scheme for reaction parameters involved in our problem**

| Function | Notation | Definition |
|---|---|---|
| Activation/Production rates | $\lambda_{XY}$ | Activation or production rate of X by Y |
| Inhibition/Removal rates | $\delta_{XY}$ | Inhibition or removal rate of X by Y |
| Natural death or decay rates | $\delta_X$ | Natural death or decay rate of X |
| Independent production rates | $A_X$ | Independent production rate of X |
| Fractions | $\alpha_{XY}$ | Fraction of X which turns into Y |
| Source rates | $S_X$ | The rate for which X is produced by its source |

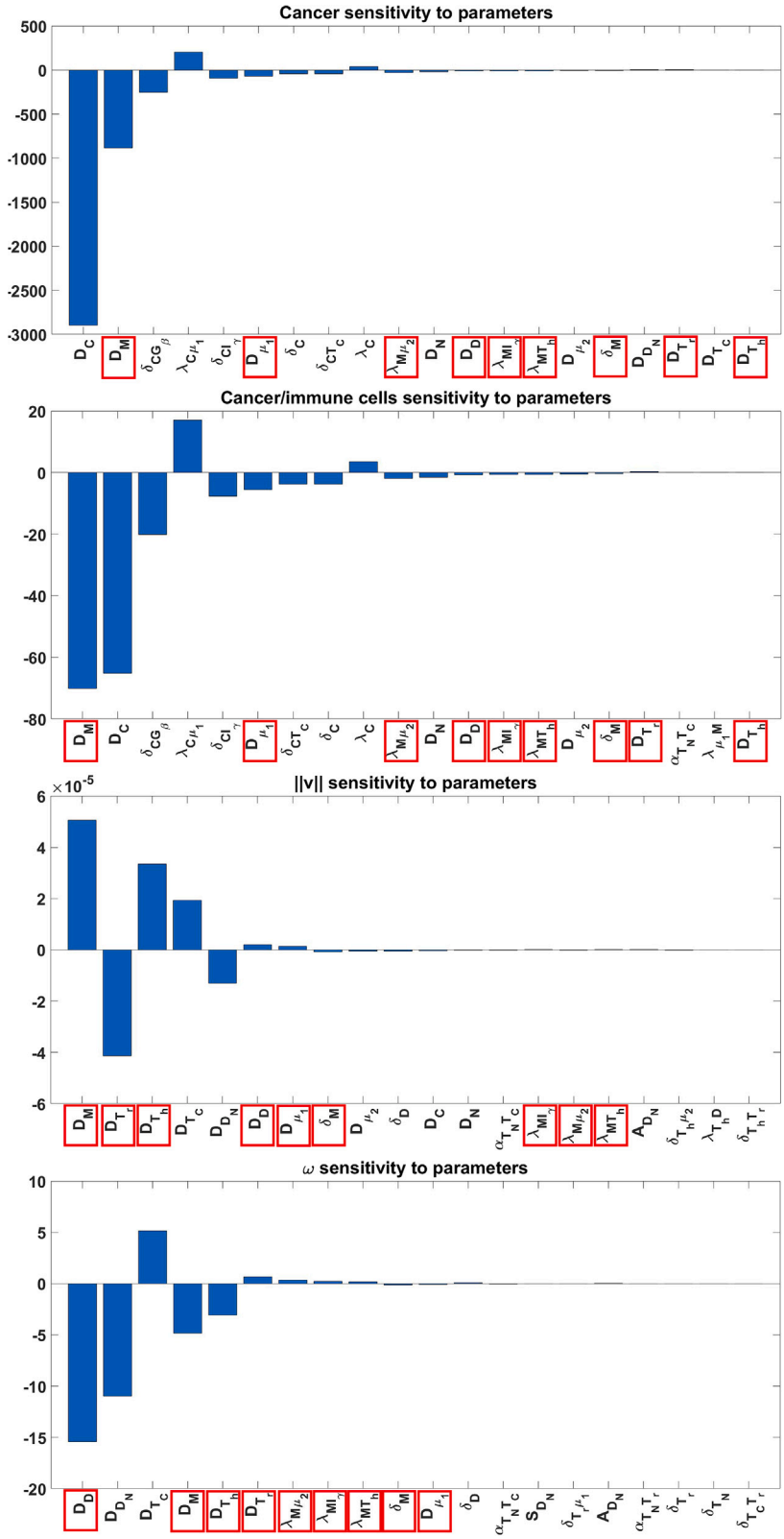
Cancer sensitivity to parameters
Cancer/immune cells sensitivity to parameters
||v|| sensitivity to parameters
ω sensitivity to parameters

**Figure 8. Adjoint-based sensitivity analysis results**

Top 20 most sensitive parameters for objective functions Equations 1, 2, 3, and 4. The parameters in red boxes are repeated in all four plots. Positive values mean that there is a direct relationship between the parameter value and the objective function value, and negative values mean an opposite correlation. The magnitude of the sensitivities is comparable within the same plot for the corresponding objective function.

creates the pink- and light blue-shaded regions for the total cancer population and cancer-immune cell ratio. The non-symmetry of these regions is expected since we perturbed the parameters that not only were sensitive for $J_1$ and $J_2$ but were also significantly sensitive for objective spatial measures $J_3$ and $J_4$.

We finish our results section by applying the model to real-world spatial data obtained from colorectal cancer patients. The data are acquired from a study by Schurch et al. in 2020.[47] In their study, they investigated 140 tissues of 35 CRC patients using formalin-fixed, paraffin-embedded (FFPE) Co-detection by indexing (CODEX) multiplexed tissue imaging to gain insight into the spatial organization of the tumor microenvironment. Using 56 protein markers, they were able to find distinct cellular neighborhoods with different immune characteristics. Their important results include colocalization of cancer with immune cell neighborhoods, fragmentation of T cells and macrophages, and worse outcomes due to the communication interruption between cellular neighborhoods. Our study agrees with their first two results. We used the data corresponding to Data S4 in the mentioned study's supplemental information. We used these data to create initial conditions for immune cells and tumor cell sources in our model. Figure 10 shows the locations of the cells in Schurch et al. study. We have included some cell types in Figure 10 that are not used in our model just for comparison. For example, we do not use B cells or non-immune cells and mixed immune cells in our model. The group of mixed immune cells is classified by $CD3^+$ biomarker expression. Since this biomarker is expressed by all T cell subtypes,[48] we titled this group mixed immune cells. The group of non-immune cells contains granulocytes, plasma cells, smooth muscle cells (SMCs), stroma, vasculature, and adipocytes, none of which are included in our model. In Kirshtein et al. and consequently, in this study, we have grouped the natural killer cells and cytotoxic T cells under one variable, namely, $T_C$. So we will combine the data for these two groups to create the source location for $T_C$ in our model. Also, Schurch et al. explore two combinations of biomarkers $CD4^+$ and $CD4^+$CD45RO+, both of which correspond to helper T cells. The difference is that the latter shows a stronger helper function for the production of antibodies.[49] Again, our model combines these biomarkers into one group of helper T cells, namely $T_h$. As for the dendritic cells, the data only consider CD11c as the biomarker, which is a biomarker expressed by immature dendritic cells.[50] So, we consider these data for $D_N$ and let the distribution of mature dendritic cells ($D$), which differentiate from $D_N$, start from zero and be decided by the dynamics of our model in time. Finally, the data consider two sets of biomarkers, $CD68^+$ and $CD68^+$CD11b+, for macrophage, which we combine for the variable $M$ in our model. We consider the model domain to be the boundary of the data; see Figure 10.

We prepare these data for our PDE model by creating a triangulated version of the domain shown by the orange curve in Figure 10. Then we count the number of cells for each model variable in each triangle and then normalize them. The result will look like Figure 11A, which represents each variable as a function in a discontinuous Galerkin function space. We then project the discontinuous functions onto a continuous linear Galerkin space and smoothen them using a pre-diffusion to avoid any irregularities caused by the projections. We, therefore, arrive at the functions shown in Figure 11B. These are ready to be fed to our PDE model for simulation.

Figure 12A shows the distribution of immune cells, necrotic cells, and cytokines after $t = 3000$ days. Figures 12B and 12C show the half-concentration contours of immune cells and cytokines super-imposed on the final distribution of cancer cells. We can again observe the fingerprint of macrophages on most cells and cytokines. More importantly, $T_C$ once again occupies the complement of the regions occupied by macrophages. In Figure 12B, we can see high values of cancer cells close to regions with high macrophage concentrations. These results qualitatively agree with our controlled experiment at the beginning of this section and show the importance of macrophages in TME spatial arrangements.

## DISCUSSION

In this study, we investigated the colon cancer tumor microenvironment spatiotemporal dynamics through a system of PDEs coupled with a linear solid elasticity problem. The reaction network and the parameters

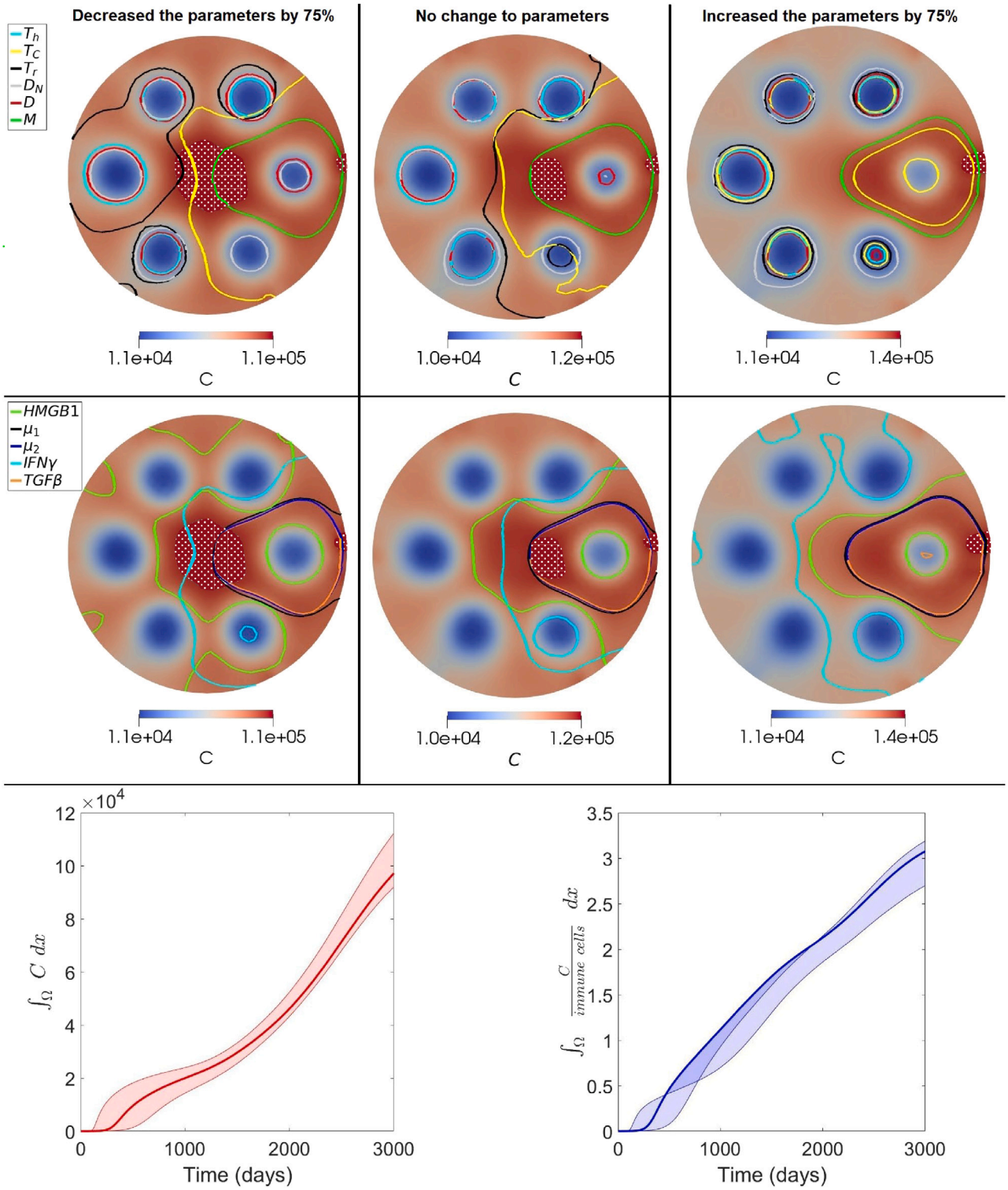


**Figure 9. Results acquired from perturbing the most common sensitive parameters**

*Top:* Changes in the half-concentration contours for cells by perturbing the common sensitive parameters by 75%. *Middle:* Changes in the half-concentration contours for molecules by perturbing the common sensitive parameters by 75%. *Bottom:* Changes in total cancer population (left) and total cancer-immune cells ratio (right) by perturbing the common sensitive parameters by 75%. The patterned regions in the top and middle figures are the regions with over 95% cancer population. These perturbations significantly affect the pattern of cell and cytokine distribution in the microenvironment.

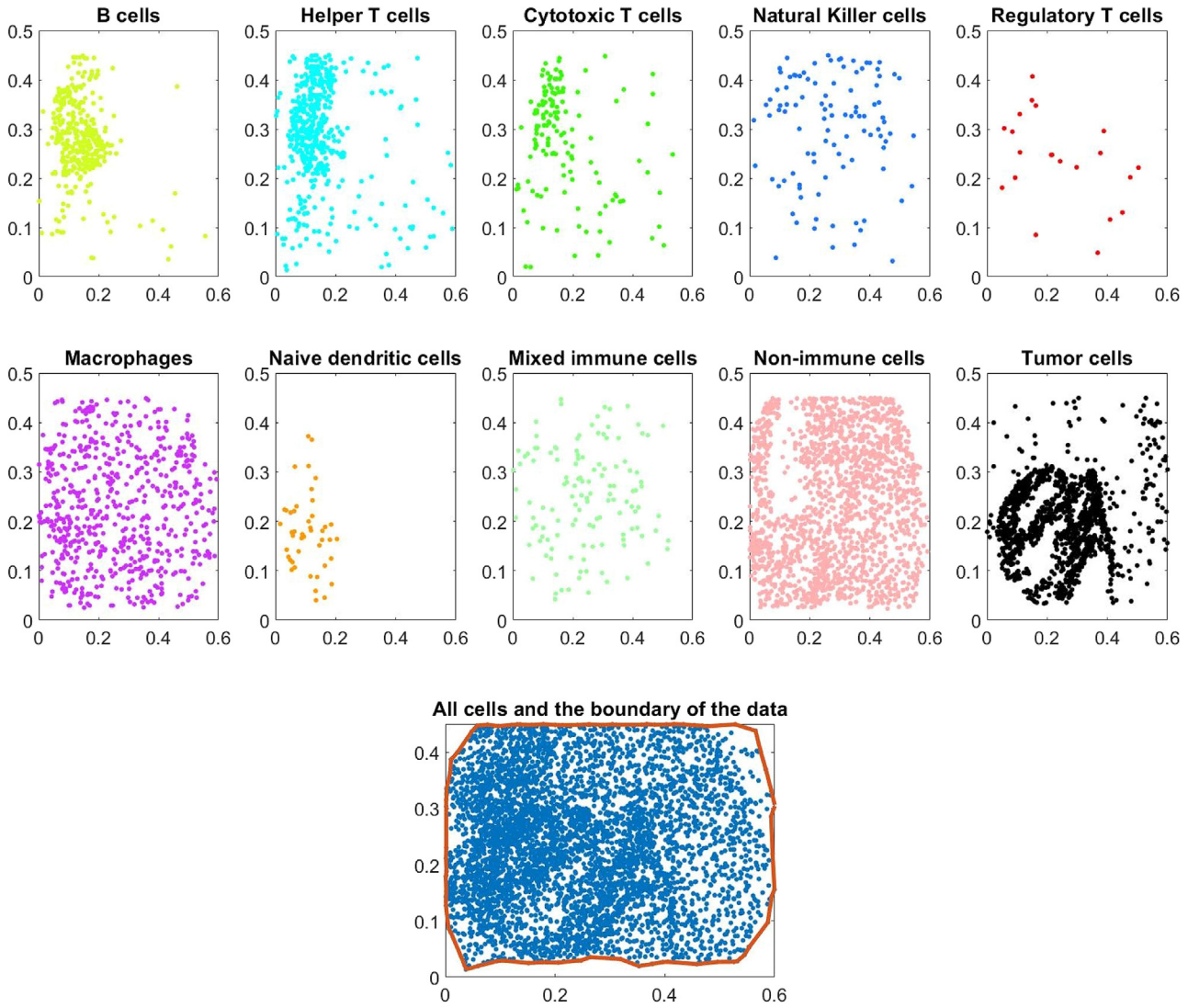


**Figure 10. Real-data location of different cell types**

Data acquired from a study by Schurch et al.[47] Some cell locations, such as B cells, Mixed immune cells, and non-immune cells, are presented for comparison with the original study and are not model variables. Mixed immune cells are $CD3^{+}$ cells, which may include all types of T cells. Non-immune cells contain granulocytes, plasma cells, smooth muscle cells (SMC), stroma, vasculature, and adipocytes. We combine natural killer cells and cytotoxic T cells as $T_C$ (see Table 1). The rest of the titles can be directly associated with model variables based on Table 1. The bottom plot shows all cells together, with the orange line marking the boundary of the data.

were extracted from an earlier study by Kirshtein et al.[28] We studied different scenarios in which we assumed separate and constant sources of immune cells within the microenvironment to provide a clearer picture of the spatial effects of immune cells inside the environment.

We used the finite element method for the simulations. We applied a mixed finite element space to search for the solution of the mechanical problem, namely the velocity $\mathbf{v}$ and pressure $p$. We then used this solution to move our triangulated domain. Next, we incorporated a mixed finite element space stabilized with bubble elements to solve for the cell and cytokine values in the moved domain. This procedure was repeated until the simulation reached $t = 3000$ days. We noticed two interesting spatial patterns formed close to the end of our simulation time: (1) circular regions at the location of the sources of the immune cells and (2) an egg-shaped region located at the right side of the domain. All the cells and cytokines were affected by these regions. Some reached their maximum and some their minimum concentration in the vicinity of these locations. We studied the probable reasons for these patterns. We think regulatory T cells (through the

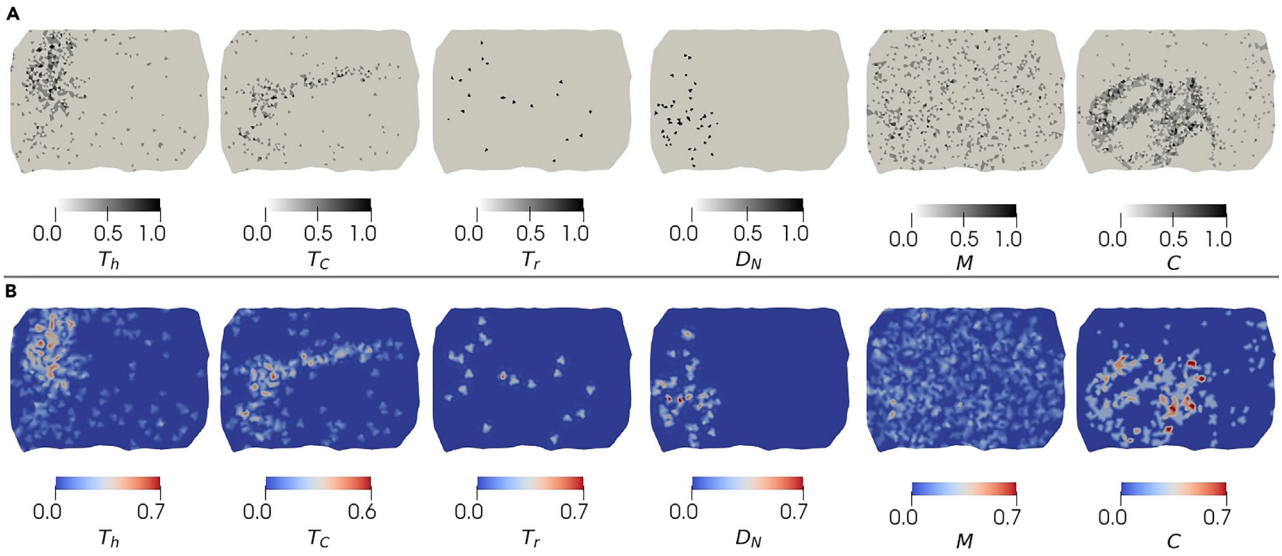


**Figure 11. Initial spatial data preparation for the PDE system**

(A) Shows the normalized discontinuous data obtained by counting the number of corresponding cells from Figure 10 in each triangle of the discretized domain.

(B) Shows the continuous data acquired by the projection of the discontinuous data functions onto a continuous linear Galerkin space and then smoothening the result using a pre-diffusion.

production of cytokines group $\mu_1$) and the outflow of the velocity field at the source locations are the reasons behind the formation of the circular regions. However, all the clues for the egg-shaped region led to macrophages. We further investigated three general cases with random immune cell sources and random domain shapes. These results confirmed that the effect of macrophages on the microenvironment spatial arrangement is independent of the location of the source of immune cells and the tumor's initial geometry. Additionally, we extracted cell location data from CODEX multiplexed tissue imaging of CRC patients' tumor microenvironment.[47] We processed the data by counting the number of cells in each triangle in our discretized domain and then projected the results onto a continuous space. This provided our model with a more realistic spatial initial condition. We observed that the patterns of most cells and cytokines were affected by macrophages, and our results were in qualitative agreement with the Schurch et al. study. Namely, we saw the colocalization of cancer and immune cells as well as the fragmentation of T cells and macrophages.

We then hypothesized that macrophage pro- and anti-tumor pathways heavily affect the tumor microenvironment spatial arrangement. To test this hypothesis, we created anti-tumor macrophages by blocking their $\mu_1$ (IL-6, IL-17, IL-21, and IL-22) production and created pro-tumor macrophages by blocking their IFN-$\gamma$ and TGF-$\beta$ production. We observed that all the major patterns were affected in the anti-tumor case. Circular regions changed their diameter for all the cells and cytokines; some even faded. Cancer and necrotic cells became more centered, and the egg-shaped regions became smaller. More importantly, cytotoxic T cells were no longer accumulated close to macrophages to be suppressed by them. As a result, we noticed better anti-tumor response by them and hence fewer cancer cells. In the pro-tumor case, most patterns persisted but with different sizes. Cytotoxic T cells were more significantly suppressed in this case; therefore, we ended up with a significantly larger population of cancer cells. This further confirms the importance of the network of interactions within the tumor microenvironment. The immune cell hubs and cross-talks between different cell types through cytokines affect both the levels and the spatial arrangement of cells, which is supported by the available literature. For example, Bocci et al. show that the sporadic localization of cancer stem cells with varying epithelial-mesenchymal transition (EMT) is related to TGF-$\beta$ and IL-6.[51] Through single-cell data analysis, Mulder et al. confirm an interaction between macrophages and $CD8^+$ T cells through IFN-$\gamma$ signaling, which leads to an immunosuppressive environment in tumors.[52] Berthel et al. also show that tumor-associated macrophages directly suppress the T cells' immune response. Through a detailed resolution analysis of T cell distribution, they notice that

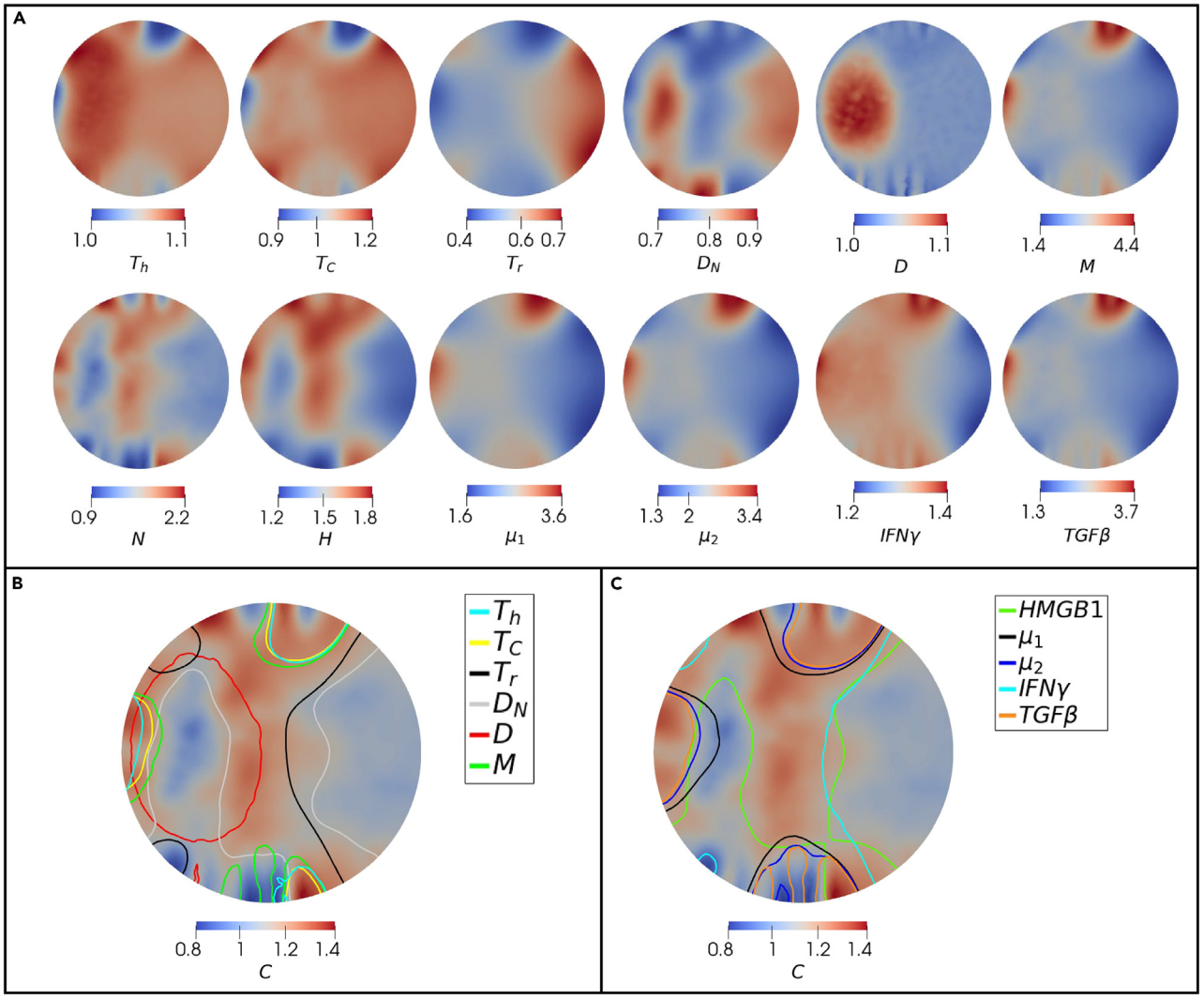


**Figure 12. Final distribution of cells and cytokines based on real-data initial conditions**

(A) Shows the distribution of immune cells, necrotic cells, and cytokines after $t$ = 3000 days. The pattern of macrophages seems to be affecting most cells and cytokines.

(B) Shows the distribution of cancer cells after $t$ = 3000 days with the half-concentration contours of immune cells. Cancer cells' population is more pronounced in the regions with high levels of macrophages.

(C) Shows the distribution of cancer cells after $t$ = 3000 days with the half-concentration contours of cytokines.

activated macrophages are proximal to cytotoxic T cells and create a physical barrier that is difficult for most T cells to overcome.[53]

To find more realistic control values rather than completely blocking the production of some cytokines, we used an adjoint-based sensitivity analysis to calculate the sensitivity of 4 objective functions to our parameters. The objective functions were total cancer population ($J_1$), total cancer-immune cell ratio ($J_2$), the total magnitude of the velocity field ($J_3$), and total angular measures of mesh points ($J_4$). We noticed that, for $J_1$, we got the same set of sensitive reaction parameters as the ODE study.[28] However, they were not the most sensitive parameters. In fact, spatial parameters such as diffusion coefficients were the most sensitive parameters for all the objective functions. Moreover, there was an abundance of macrophage-related sensitive parameters for all four cases, which was in line with our speculations. We picked a set of 9 parameters introduced in all four cases as sensitive and perturbed them by 75%. We expected a significant change in the common spatial patterns and total cancer and cancer-immune cell ratio, and we were not disappointed. There were significant changes in the diameter of the circular regions and the area of the egg-shaped

region. In addition, we saw drastic changes in the contours representing the half-concentration of cells and cytokines such as $T_r$, $T_C$, $M$, *HMGB*1, and IFN-$\gamma$. The high-concentration regions of the cancer population also shifted from the center of the domain to a boundary-adjacent region at 3 o'clock. The confidence interval for the total cancer population and the cancel-immune cell ratio was also affected but in a non-symmetric fashion. This was due to changing parameters that affected these two measures and had a significant spatial impact.

Given the flexibility of mathematical experiments, we could create a situation that might not be feasible experimentally. However, the results from this study can help scientists design specific targeted lab experiments. For example, we noticed an exciting colocalization pattern between macrophages and cytotoxic T cells. Cytotoxic T cells were quickly recruited to the site of macrophages in the case of pro-tumor-dominated macrophages. Moreover, it was visually observable that macrophages prevented the contact between cytotoxic cells and cancer cells. This effect was almost wholly obviated when we changed the macrophages to anti-tumor. While the suppression of anti-tumor immunity by M2 (pro-tumor) macrophages in the microenvironment is discussed in the field,[16–18] how they do it is widely unknown.[54] We must also emphasize that our model does not include chemotaxis, durotaxic, or similar effects. These spatial recruitment and suppression effects are created mainly by simple mass action laws. This attests to the necessity of investigating the tumor microenvironment interactions as detailed as possible. In addition, we saw that activation rates of macrophages (when both anti-tumor and pro-tumor macrophages were included) by IFN-$\gamma$, $T_h$, and $\mu_2$ (including IL-10 and CCL20) are important control parameters for controlling the concentration and pattern of most cells and cytokines, especially cancer cells. It has been seen that high levels of macrophages lead to better prognoses for colon cancer.[55,56] On the other hand, we saw that the natural death of macrophages also leads to less cancer population. Interestingly, it has also been confirmed that lower levels of macrophages are better for colorectal patients.[57,58] It is hypothesized that co-treatment of patients by balancing the macrophage activation and the cytotoxicity of the tumor can be of great importance.[59] This is due to the delicate balance of macrophages in CRC that can go either way based on the differences in tumor microenvironments and gene profiles of different patients.[60]

In this paper, we used static data acquired from CRC patients using CODEX multiplexed tissue imaging for characterizing cell neighborhoods conducted by Schűrch et al. While we understand that a time course validation of these results for humans might be very difficult, genetically engineered mouse models or *in vitro* models of CRC can be useful to get insight into tumors' development and progression. Although both models have the same disadvantage of lacking invasiveness, metastasis, and tumor heterogeneity compared to human CRC,[61] they both have more flexibility in activating or inhibiting certain molecular pathways. For example, using an $Apc^{Min/+}$ mouse model, Nakanishi et al. discover that cyclooxygenase-2 (COX-2) inhibition positively affects the polarization from M2 to M1 macrophages accompanied by increased IFN-$\gamma$ production.[62] In another study, Smith et al. investigate the hysteresis-like behavior of macrophage polarization using *in vitro* assays and polarization stimuli such as Lipopolysaccharide (LPS) or IFN $\gamma$ and IL-4 or IL-13 as inputs.[47,63] We hope our study can motivate similar longitudinal experiments to unveil the most responsible pathways for the spatial arrangement of the tumor microenvironment.

### Limitations of the study

We acknowledge that this study comes with various limitations. To reduce the burden of parameter estimation and avoid too much complexity, we tried to stay faithful to an earlier ODE study.[28] Therefore, we refrained from adding new variables to the models, such as metabolites, fibroblasts, oxygen, etc. These factors play an essential role in the development and progression of cancer.[64–66] Additionally, for simplicity, we assumed linear elasticity for this problem; but colon tissue and colon cancer might follow non-linear elastic behaviors.[67] Finally, our diffusion coefficients can have more realistic interpretations. For example, we can include a necrotic core that affects the value of the diffusion coefficients for cells and cytokines. In the future, we plan to prevent as many limitations as possible and include therapy. We hope to show that the spatial arrangement of the tumor microenvironment and drug administration significantly impact cancer treatment.

## STAR★METHODS

Detailed methods are provided in the online version of this paper and include the following:

- KEY RESOURCES TABLE

## SUPPLEMENTAL INFORMATION

Supplemental information can be found online at https://doi.org/10.1016/j.isci.2023.106596.

## ACKNOWLEDGMENTS

Research reported in this publication was partially supported by the National Cancer Institute of the National Institutes of Health under Award Number R21CA242933. WH was partially supported by the National Institute of General Medical Sciences under Award Number 1R35GM146894. The content is solely the responsibility of the authors and does not necessarily represent the official views of the National Institutes of Health.

## AUTHOR CONTRIBUTIONS

N.M. and L.S. designed the study; N.M. conceived and conducted the experiments; N.M., W.H., and L.S. developed the model; N.M. and L.S. analyzed the results; N.M. wrote the manuscript; L.S. supervised the project. All authors reviewed the manuscript.

## DECLARATION OF INTERESTS

The authors declare no competing interests.

Received: August 24, 2022
Revised: February 28, 2023
Accepted: April 3, 2023
Published: April 10, 2023

## REFERENCES

1. Ferlay, J., Ervik, M., Lam, F., Colombet, M., Mery, L., Piñeros, M., Znaor, A., Soerjomataram, I., and Bray, F. (2020). Global Cancer Observatory: Cancer Today (International Agency for Research on Cancer). https://gco.iarc.fr/today.

2. Ahmed, M. (2020). Colon cancer: a clinician's perspective in 2019. Gastroenterology Res. *13*, 1–10. https://doi.org/10.14740/gr1239.

3. Buccafusca, G., Proserpio, I., Tralongo, A.C., Rametta Giuliano, S., and Tralongo, P. (2019). Early colorectal cancer: diagnosis, treatment and survivorship care. Crit. Rev. Oncol. Hematol. *136*, 20–30. https://doi.org/10.1016/j.critrevonc.2019.01.023.

4. Ciardiello, D., Vitiello, P.P., Cardone, C., Martini, G., Troiani, T., Martinelli, E., and Ciardiello, F. (2019). Immunotherapy of colorectal cancer: challenges for therapeutic efficacy. Cancer Treat Rev. *76*, 22–32. https://doi.org/10.1016/j.ctrv.2019.04.003.

5. Häfner, M.F., and Debus, J. (2016). Radiotherapy for colorectal cancer: current standards and future perspectives. Visc. Med. *32*, 172–177. https://doi.org/10.1159/000446486.

6. Xie, Y.-H., Chen, Y.-X., and Fang, J.-Y. (2020). Comprehensive review of targeted therapy for colorectal cancer. Signal Transduct. Target. Ther. *5*, 22. https://doi.org/10.1038/s41392-020-0116-z.

7. Abulafi, A.M., and Williams, N.S. (1994). Local recurrence of colorectal cancer: the problem, mechanisms, management and adjuvant therapy. Br. J. Surg. *81*, 7–19. https://doi.org/10.1002/bjs.18008101 06.

8. Stintzing, S. (2014). Management of colorectal cancer. F1000Prime Rep. *6*, 108. https://doi.org/10.12703/P6-108.

9. Mahvi, D.A., Liu, R., Grinstaff, M.W., Colson, Y.L., and Raut, C.P. (2018). Local cancer recurrence: the realities, challenges, and opportunities for new therapies. CA. Cancer J. Clin. *68*, 488–505. https://doi.org/10.3322/caac.21498.

10. Anderson, N.M., and Simon, M.C. (2020). The tumor microenvironment. Curr. Biol. *30*, R921–R925. https://doi.org/10.1016/j.cub.2020.06.081.

11. Multhoff, G., Molls, M., and Radons, J. (2011). Chronic inflammation in cancer development. Front. Immunol. *2*, 98. https://doi.org/10.3389/fimmu.2011.00098.

12. Chai, E.Z.P., Siveen, K.S., Shanmugam, M.K., Arfuso, F., and Sethi, G. (2015). Analysis of the intricate relationship between chronic inflammation and cancer. Biochem. J. *468*, 1–15. https://doi.org/10.1042/BJ20141337.

13. Zamarron, B.F., and Chen, W. (2011). Dual roles of immune cells and their factors in cancer development and progression. Int. J. Biol. Sci. *7*, 651–658. https://doi.org/10.7150/ijbs.7.651.

14. Pan, X.-Q. (2012). The mechanism of the anticancer function of M1 macrophages and their use in the clinic. Chin. J. Cancer *31*, 557–563. https://doi.org/10.5732/cjc.012.10046.

15. Edin, S., Wikberg, M.L., Oldenborg, P.A., and Palmqvist, R. (2013). Macrophages: good guys in colorectal cancer. Oncolmmunology *2*, e23038. https://doi.org/10.4161/onci.23038.

16. Kruse, J., von Bernstorff, W., Evert, K., Albers, N., Hadlich, S., Hagemann, S., Günther, C., van Rooijen, N., Heidecke, C.D., and Partecke, L.I. (2013). Macrophages promote tumour growth and liver metastasis in an orthotopic syngeneic mouse model of colon cancer. Int. J. Colorectal Dis. *28*, 1337–1349. https://doi.org/10.1007/s00384-013-1703-z.

17. Pollard, J.W. (2004). Tumour-educated macrophages promote tumour progression and metastasis. Nat. Rev. Cancer *4*, 71–78. https://doi.org/10.1038/nrc1256.

18. Bingle, L., Brown, N.J., and Lewis, C.E. (2002). The role of tumour-associated macrophages in tumour progression: implications for new anticancer therapies. J. Pathol. *196*, 254–265. https://doi.org/10.1002/path.1027.

19. Peranzoni, E., Lemoine, J., Vimeux, L., Feuillet, V., Barrin, S., Kantari-Mimoun, C., Bercovici, N., Guérin, M., Biton, J., Ouakrim, H., et al. (2018). Macrophages impede CD8 T cells from reaching tumor cells and limit the efficacy of anti-PD-1 treatment. Proc. Natl. Acad. Sci. USA *115*, E4041–E4050. https://doi.org/10.1073/pnas.1720948115.

20. Isidro, R.A., and Appleyard, C.B. (2016). Colonic macrophage polarization in homeostasis, inflammation, and cancer. Am. J. Physiol. Gastrointest. Liver Physiol. *311*, G59–G73. https://doi.org/10.1152/ajpgi.00123.2016.

21. Yuan, Y. "Spatial Heterogeneity in the Tumor Microenvironment" https://doi.org/10.1101/cshperspect.a026583.

22. Shahriyari, L., Komarova, N.L., and Jilkine, A. (2016). The role of cell location and spatial gradients in the evolutionary dynamics of colon and intestinal crypts. Biol. Direct *11*, 42. https://doi.org/10.1186/s13062-016-0141-6.

23. Zheng, X., Weigert, A., Reu, S., Guenther, S., Mansouri, S., Bassaly, B., Gattenlöhner, S., Grimminger, F., Pullamsetti, S., Seeger, W., et al. (2020). Spatial density and distribution of tumor-associated macrophages predict survival in non-small cell lung CarcinomaTumor- associated macrophage subtypes in lung cancer. Cancer Res. *80*, 4414–4425. https://doi.org/10.1158/0008-5472.CAN-20-0069.

24. Nielsen, J.S., Sahota, R.A., Milne, K., Kost, S.E., Nesslinger, N.J., Watson, P.H., and Nelson, B.H. (2012). CD20+ tumor-infiltrating lymphocytes have an atypical CD27- memory phenotype and together with CD8+ T cells promote favorable prognosis in ovarian CancerCD20+ TIL promote favorable prognosis in ovarian cancer. Clin. Cancer Res. *18*, 3281–3292. https://doi.org/10.1158/1078-0432.CCR-12-0234.

25. Galon, J., Costes, A., Sanchez-Cabo, F., Kirilovsky, A., Mlecnik, B., Lagorce-Pagès, C., Tosolini, M., Camus, M., Berger, A., Wind, P., et al. (2006). Type, density, and location of immune cells within human colorectal tumors predict clinical outcome. Science *313*, 1960–1964. https://doi.org/10.1126/science.1129139.

26. Trédan, O., Galmarini, C.M., Patel, K., and Tannock, I.F. (2007). Drug resistance and the solid tumor microenvironment. J. Natl. Cancer Inst. *99*, 1441–1454. https://doi.org/10.1093/jnci/djm135.

27. Dritschel, H., Waters, S., Roller, A., and Byrne, H. (2018). A mathematical model of cytotoxic and helper T cell interactions in a tumor microenvironment. Lett. Biomath. *5*. https://doi.org/10.30707/LiB5.2Dritschel.

28. Kirshtein, A., Akbarinejad, S., Hao, W., Le, T., Su, S., Aronow, R.A., and Shahriyari, L. (2020). Data driven mathematical model of colon cancer progression. J. Clin. Med. *9*, 3947. https://doi.org/10.3390/jcm9123947.

29. Le, T., Su, S., Kirshtein, A., and Shahriyari, L. (2021). Data-driven mathematical model of osteosarcoma. Cancers *13*, 2367. https://doi.org/10.3390/cancers13 102367.

30. Le, T., Su, S., and Shahriyari, L. (2021). Investigating optimal chemotherapy options for osteosarcoma patients through a mathematical model. Cells *10*, 2009. https://doi.org/10.3390/cells1008 2009.

31. Budithi, A., Su, S., Kirshtein, A., and Shahriyari, L. (2021). Data driven mathematical model of FOLFIRI treatment for colon cancer. Cancers *13*, 2632. https://doi.org/10.3390/cancers13112632.

32. Mohammad Mirzaei, N., Su, S., Sofia, D., Hegarty, M., Abdel-Rahman, M.H., Asadpoure, A., Cebulla, C.M., Chang, Y.H., Hao, W., Jackson, P.R., et al. (2021). A mathematical model of breast tumor progression based on immune infiltration. J. Pers. Med. *11*, 1031. https://doi.org/10.3390/jpm11101031.

33. Mohammad Mirzaei, N., Changizi, N., Asadpoure, A., Su, S., Sofia, D., Tatarova, Z., Zervantonakis, I.K., Chang, Y.H., and Shahriyari, L. (2022). Investigating key cell types and molecules dynamics in PyMT mice model of breast cancer through a mathematical model. PLoS Comput. Biol. *18*, e1009953. https://doi.org/10.1371/journal.pcbi.1009953.

34. Kim, Y., and Friedman, A. (2010). Interaction of tumor with its micro-environment: a mathematical model. Bull. Math. Biol. *72*, 1029–1068. https://doi.org/10.1007/s11538-009-9481-z.

35. Mohammad Mirzaei, N., Tatarova, Z., Hao, W., Changizi, N., Asadpoure, A., Zervantonakis, I.K., Hu, Y., Chang, Y.H., and Shahriyari, L. (2022). A PDE model of breast tumor progression in MMTV-PyMT mice. J. Pers. Med. *12*, 807. https://doi.org/10.3390/jpm12050807.

36. Owen, M.R., and Sherratt, J.A. (1997). Pattern formation and spatiotemporal irregularity in a model for macrophage-tumour interactions. J. Theor. Biol. *189*, 63–80. https://doi.org/10.1006/jtbi.199 7.0494.

37. Araujo, R.P., and McElwain, D.L.S. (2004). A linear-elastic model of anisotropic tumour growth. Eur. J. Appl. Math. *15*, 365–384. https://doi.org/10.1017/S0956792504005406.

38. Shannon, M., and Rubinsky, B. (1993). The Effect of Tumor Growth on the Stress Distribution in Tissue, *231* (ASME-PUBLICATIONS-HTD), p. 35.

39. Roose, T., Netti, P.A., Munn, L.L., Boucher, Y., and Jain, R.K. (2003). Solid stress generated by spheroid growth estimated using a linear poroelasticity model. Microvasc. Res. *66*, 204–212. https://doi.org/10.1016/S0026-2862(03)00057-8.

40. Jones, A.F., Byrne, H.M., Gibson, J.S., and Dold, J.W. (2000). A mathematical model of the stress induced during avascular tumour growth. J. Math. Biol. *40*, 473–499. https://doi.org/10.1007/s002850000033.

41. Liao, K.-L., Bai, X.-F., and Friedman, A. (2014). Mathematical modeling of interleukin-27 induction of anti-tumor T cells response. PLoS One *9*, e91844. https://doi.org/10.1371/journal.pone.0091844.

42. Hao, W., and Friedman, A. (2016). Mathematical model on Alzheimer's disease. BMC Syst. Biol. *10*, 108. https://doi.org/10.1186/s12918-016-0348-2.

43. Liao, K.-L., Bai, X.-F., and Friedman, A. (2013). The role of CD200-CD200R in tumor immune evasion. J. Theor. Biol. *328*, 65–76. https://doi.org/10.1016/j.jtbi.2013.03.017.

44. Kusume, A., Sasahira, T., Luo, Y., Isobe, M., Nakagawa, N., Tatsumoto, N., Fujii, K., Ohmori, H., and Kuniyasu, H. (2009). Suppression of dendritic cells by HMGB1 is associated with lymph node metastasis of human colon cancer. Pathobiology *76*, 155–162. https://doi.org/10.1159/000218331.

45. Kim, H.-J., and Cantor, H. (2014). CD4 T-cell subsets and tumor immunity: the helpful and the not-so-helpful. Cancer Immunol. Res. *2*, 91–98. https://doi.org/10.1158/2326-6066.CIR-13-0216.

46. Fu, C., and Jiang, A. (2018). Dendritic cells and CD8 T cell immunity in tumor microenvironment. Front. Immunol. *9*, 3059. https://doi.org/10.3389/fimmu.2018.03059.

47. Schürch, C.M., Bhate, S.S., Barlow, G.L., Phillips, D.J., Noti, L., Zlobec, I., Chu, P., Black, S., Demeter, J., McIlwain, D.R., et al. (2020). Coordinated cellular neighborhoods orchestrate antitumoral immunity at the colorectal cancer invasive front. Cell *182*, 1341–1359. https://doi.org/10.1016/j.cell.2020.07.005.

48. Tatarova, Z., Blumberg, D.C., Korkola, J.E., Heiser, L.M., Muschler, J.L., Schedin, P.J., Ahn, S.W., Mills, G.B., Coussens, L.M., Jonas, O., and Gray, J.W. (2022). A multiplex implantable microdevice assay identifies synergistic combinations of cancer immunotherapies and conventional drugs.

Nat. Biotechnol. *40*, 1823–1833. https://doi.org/10.1038/s4 1587-022-01379-y.

49. Devi, M., Vijayalakshmi, D., Dhivya, K., and Janane, M. (2017). Memory T cells (CD45RO) role and evaluation in pathogenesis of lichen planus and lichenoid mucositis. J. Clin. Diagn. Res. *11*, ZC84–ZC86. https://doi.org/10.7860/JCDR/2017/26866.9930.

50. Schraml, B.U., and Reis e Sousa, C. (2015). Defining dendritic cells. Curr. Opin. Immunol. *32*, 13–20. https://doi.org/10.1016/j.coi.20 14.11.001.

51. Bocci, F., Gearhart-Serna, L., Boareto, M., Ribeiro, M., Ben-Jacob, E., Devi, G.R., Levine, H., Onuchic, J.N., and Jolly, M.K. (2019). Toward understanding cancer stem cell heterogeneity in the tumor microenvironment. Proc. Natl. Acad. Sci. USA *116*, 148–157. https://doi.org/10.1073/pnas.1815345116.

52. Mulder, K., Patel, A.A., Kong, W.T., Piot, C., Halitzki, E., Dunsmore, G., Khalilnezhad, S., Irac, S.E., Dubuisson, A., Chevrier, M., et al. (2021). Cross-tissue single-cell landscape of human monocytes and macrophages in health and disease. Immunity *54*, 1883–1900.e5. https://doi.org/10.1016/j.immuni.2021.07.007.

53. Berthel, A., Zoernig, I., Valous, N.A., Kahlert, C., Klupp, F., Ulrich, A., Weitz, J., Jaeger, D., and Halama, N. (2017). Detailed resolution analysis reveals spatial T cell heterogeneity in the invasive margin of colorectal cancer liver metastases associated with improved survival. OncoImmunology *6*, e1286436. https://doi.org/10.1080/2162402X.2017.1286436.

54. Petty, A.J., Li, A., Wang, X., Dai, R., Heyman, B., Hsu, D., Huang, X., and Yang, Y. (2019). Hedgehog signaling promotes tumor-associated macrophage polarization to suppress intratumoral CD8+ T cell recruitment. J. Clin. Invest. *129*, 5151–5162. https://doi.org/10.1172/JCI128644.

55. Oosterling, S.J., van der Bij, G.J., Meijer, G.A., Tuk, C.W., van Garderen, E., van Rooijen, N., Meijer, S., van der Sijp, J.R.M., Beelen, R.H.J., and van Egmond, M. (2005). Macrophages direct tumour histology and clinical outcome in a colon cancer model. J. Pathol. *207*, 147–155. https://doi.org/10.1002/path.1830.

56. Bindea, G., Mlecnik, B., Tosolini, M., Kirilovsky, A., Waldner, M., Obenauf, A.C., Angell, H., Fredriksen, T., Lafontaine, L., Berger, A., et al. (2013). Spatiotemporal dynamics of intratumoral immune cells reveal the immune landscape in human cancer. Immunity *39*, 782–795. https://doi.org/10.1016/j.immuni.2013.10.003.

57. Erreni, M., Mantovani, A., and Allavena, P. (2011). Tumor-associated macrophages (TAM) and inflammation in colorectal cancer. Cancer Microenviron. *4*, 141–154. https://doi.org/10.1007/s12307-010-0052-5.

58. Wang, W., Li, X., Zheng, D., Zhang, D., Peng, X., Zhang, X., Ai, F., Wang, X., Ma, J., Xiong, W., et al. (2015). Dynamic changes and functions of macrophages and M1/M2 subpopulations during ulcerative colitis-associated carcinogenesis in an AOM/DSS mouse model. Mol. Med. Rep. *11*, 2397–2406. https://doi.org/10.3892/mmr.2014.3018.

59. Klimp, A.H., de Vries, E.G.E., Scherphof, G.L., and Daemen, T. (2002). A potential role of macrophage activation in the treatment of cancer. Crit. Rev. Oncol. Hematol. *44*, 143–161. https://doi.org/10.1016/S1040-8428(01)00203-7.

60. Braster, R., Bögels, M., Beelen, R.H.J., and van Egmond, M. (2017). The delicate balance of macrophages in colorectal cancer; their role in tumour development and therapeutic potential. Immunobiology *222*, 21–30. https://doi.org/10.1016/j.imbio.2015.08.011.

61. Bürtin, F., Mullins, C.S., and Linnebacher, M. (2020). Mouse models of colorectal cancer: past, present and future perspectives. World J. Gastroenterol. *26*, 1394. https://doi.org/10.3748/wjg.v26.i13.1394.

62. Nakanishi, Y., Nakatsuji, M., Seno, H., Ishizu, S., Akitake-Kawano, R., Kanda, K., Ueo, T., Komekado, H., Kawada, M., Minami, M., and Chiba, T. (2011). COX-2 inhibition alters the phenotype of tumorassociated macrophages from M2 to M1 in Apc Min/+ mouse polyps. Carcinogenesis *32*, 1333–1339. https://doi.org/10.1093/carcin/bgr128.

63. Smith, T.D., Tse, M.J., Read, E.L., and Liu, W.F. (2016). Regulation of macrophage polarization and plasticity by complex activation signals. Integr. Biol. *8*, 946–955. https://doi.org/10.1039/c6ib00105j.

64. Mukaida, N., and Sasaki, S. (2016). Fibroblasts, an inconspicuous but essential player in colon cancer development and progression. World J. Gastroenterol. *22*, 5301–5316. https://doi.org/10.3748/wjg.v22.i23.5 301.

65. Reddy, B.S. (1975). Role of bile metabolites in colon carcinogenesis. *Animal models*. Cancer *36*, 2401–2406. https://doi.org/10.1002/1097-0142(197512)36:6<2401::AID-CNCR2820360619>3.0.CO;2-O.

66. Salim, A.S. (1993). The permissive role of oxygen-derived free radicals in the development of colonic cancer in the rat. A new theory for carcinogenesis. Int. J. Cancer *53*, 1031–1035. https://doi.org/10.1002/ijc.2910530629.

67. Carniel, E.L., Gramigna, V., Fontanella, C.G., Stefanini, C., and Natali, A.N. (2014). Constitutive formulations for the mechanical investigation of colonic tissues. J. Biomed. Mater. Res. *102*, 1243–1254. https://doi.org/10.1002/jbm.a.34787.

68. Logg, A., Mardal, K.-A., and Wells, G. (2012). Automated Solution of Differential Equations by the Finite Element Method: The FEniCS Book. https://doi.org/10.1007/978-3-642-23099. 84.

69. Geuzaine, C., and Remacle, J.-F. (2009). Gmsh: a 3-D finite element mesh generator with built-in pre-and post-processing facilities. Int. J. Numer. Methods Eng. *79*, 1309–1331. https://doi.org/10.1002/nme.2579.

70. Engelhardt, J.J., Boldajipour, B., Beemiller, P., Pandurangi, P., Sorensen, C., Werb, Z., Egeblad, M., and Krummel, M.F. (2012). Marginating dendritic cells of the tumor microenvironment cross-present tumor antigens and stably engage tumorspecific T cells. Cancer Cell *21*, 402–417. https://doi.org/10.1016/j .ccr.2012.01.008.

71. Maimela, N.R., Liu, S., and Zhang, Y. (2019). Fates of CD8+ T cells in tumor microenvironment. Comput. Struct. Biotechnol. J. *17*, 1–13. https://doi.org/10.1016/j.csbj.2018.11.004.

72. Randolph, G.J., Ivanov, S., Zinselmeyer, B.H., and Scallan, J.P. (2017). The lymphatic system: integral roles in immunity. Annu. Rev. Immunol. *35*, 31–52. https://doi.org/10.1146/a nnurev-immunol-041015-055354.

73. Michielsen, A.J., Noonan, S., Martin, P., Tosetto, M., Marry, J., Biniecka, M., Maguire, A.A., Hyland, J.M., Sheahan, K.D., O'Donoghue, D.P., et al. (2012). Inhibition of dendritic cell maturation by the tumor microenvironment correlates with the survival of colorectal cancer patients following bevacizumab treatment. Mol. Cancer Ther. *11*, 1829–1837. https://doi.org/10.1158/1535-7163.MCT-1 2-0162.

74. Gabrilovich, D. (2004). Mechanisms and functional significance of tumourinduced dendritic-cell defects. Nat. Rev. Immunol. *4*, 941–952. https://doi.org/10.1038/nri1498.

75. Ramos, J.I. (2009). Picard's iterative method for nonlinear advection-reaction- diffusion equations. Appl. Math. Comput. *215*, 1526–1536. https://doi.org/10.1016/j.amc.2009.07.004.

76. Franks, S.J., Byrne, H.M., King, J.R., Underwood, J.C.E., and Lewis, C.E. (2003). Modelling the early growth of ductal carcinoma in situ of the breast. J. Math. Biol. *47*, 424–452. https://doi.org/10.1007/s00285-003-0214-x.

77. Friedman, A., and Hu, B. (2007). Bifurcation for a free boundary problem modeling tumor growth by Stokes equation. SIAM J. Math. Anal. *39*, 174–194. https://doi.org/10.1137/060656292.

78. Hao, W., and Friedman, A. (2014). The LDL-HDL profile determines the risk of atherosclerosis: a mathematical model. PLoS One *9*, e90497. https://doi.org/10.1371/journal.pone.0090497.

79. Hasgall, P., Di Gennaro, F., Baumgartner, C., Neufeld, E., Lloyd, B., Gosselin, M.C., Payne, D., Klingenböck, A., and Kuster, N. (2022). IT'IS Database for Thermal and Electromagnetic Parameters of Biological Tissues, Version 4.1 (IT'IS). https://doi.org/10.13099/VIP21000-04-1.

80. Fung, Y.-C., and Drucker, D.C. (1966). Foundation of solid mechanics. J. Appl. Mech. *33*, 238. https://doi.org/10.1115/1.3625018.

81. Irgens, F. (2008). Continuum Mechanics. https://doi.org/10.1007/978-3-540-74298-2.

82. Sancho, A., Vandersmissen, I., Craps, S., Luttun, A., and Groll, J. (2017). A new strategy to measure intercellular adhesion forces in mature cell-cell contacts. Sci. Rep. *7*, 46152. https://doi.org/10.1038/srep46152.

83. Deptuła, P., Łysik, D., Pogoda, K., Cieśluk, M., Namiot, A., Mystkowska, J., Król, G., Głuszek, S., Janmey, P.A., and Bucki, R. (2020). Tissue rheology as a possible complementary procedure to advance histological diagnosis of colon cancer. ACS Biomater. Sci. Eng. *6*, 5620–5631. https://doi.org/10.1021/acsbiomaterials.0c00975.

84. Solonnikov, V. (1999). On quasistationary approximation in the problem of motion of a capillary drop. Top. Nonlinear Anal. 643–671. https://doi.org/10.1007/978-3-0348-8765-6_28.

85. Vainberg, M., and Trenogin, V. (1974). Theory of Branching Solutions of Nonlinear Equations (Leyden: Noordhoff International Pub). https://doi.org/10.1090/S0002-9904-1975-13871-7.

86. Gander, M.J., and Kwok, F. (2018). Numerical Analysis of Partial Differential Equations Using Maple and MATLAB. https://doi.org/10.1137/1.9781611975314.bm.

87. Brezzi, F., and Russo, A. (1994). Choosing bubbles for advection-diffusion problems. Math. Models Methods Appl. Sci. *4*, 571–587. https://doi.org/10.1142/S0218202594000327.

88. Franca, L.P., Nesliturk, A., and Stynes, M. (1998). On the stability of residualfree bubbles for convection-diffusion problems and their approximation by a two-level finite element method. Comput. Methods Appl. Mech. Eng. *166*, 35–49. https://doi.org/10.1016/S0045-7825(98)00081-4.

89. Sendur, A. (2018). A comparative study on stabilized finite element methods for the convection-diffusion-reaction problems. J. Appl. Math. *2018*, 1–16. https://doi.org/10.1155/2018/4259634.

90. Li, S., and Petzold, L. (2004). Adjoint sensitivity analysis for time-dependent partial differential equations with adaptive mesh refinement. J. Comput. Phys. *198*, 310–325. https://doi.org/10.1016/j.jcp.2003.01.001.

91. Mitusch, S., Funke, S., and Dokken, J. (2019). dolfin-adjoint 2018.1: automated adjoints for FEniCS and Firedrake. J. Open Source Softw. *4*, 1292. https://doi.org/10.21105/joss.01292.

# STAR★METHODS

## KEY RESOURCES TABLE

| REAGENT or RESOURCE | SOURCE | IDENTIFIER |
|---|---|---|
| Software and algorithms | | |
| Python 3.7 | Python Software Foundation | www.python.org/downloads/ |
| FEniCS (2019.2.0.dev0) | Logg et al. (2012)[68] | www.fenicsproject.org/download/ |
| MATLAB (R2021b) | The MathWork, Inc. | www.mathworks.com/products/matlab.html |
| GMSH (3.0.4) | Geuzaine et al. (2009)[69] | www.gmsh.info/#Download |
| Paraview (5.10.0) | Kitware, Inc. | www.paraview.org/download/ |
| Simulation results and codes | this paper | www.github.com/ShahriyariLab/Investigating-the-spatial-interaction-of-immune-cells-in-colon-cancer |

## RESOURCE AVAILABILITY

### Lead contact

Further questions should be directed to and will be answered by the Lead Contact, Leili Shahriyari (lshahriyari@umass.edu).

### Materials availability

This study did not utilize any physical material.

### Data and code availability

All the codes and data are available at https://github.com/ShahriyariLab/Investigating-the-spatial-interaction-of-immune-cells-in-colon-cancer. Any additional information required to reanalyze the data reported in this paper is available from the lead contact upon request.

## METHOD DETAILS

### The ODE model

The model includes 14 variables denoted by the state variable vector $[\mathbf{X}] = ([X_1],[X_2],\ldots,[X_{14}])$, see Table 1 for the definition of each variable.

The following is the system of ODEs used by Kirshtein et al.[28]

$$\frac{d[T_N]}{dt} = A_{T_N} - \left(\lambda_{T_hD}[D] + \lambda_{T_hM}[M] + \lambda_{T_h\mu_1}[\mu_1]\right)[T_N] - \left(\lambda_{T_CT_h}[T_h] + \lambda_{T_CD}[D]\right)[T_N] - \left(\lambda_{T_rT_h}[T_h] + \lambda_{T_r\mu_2}[\mu_2] + \lambda_{T_rG_\beta}[G_\beta]\right)[T_N] - \delta_{T_N}[T_N] \quad \text{(Equation 5)}$$

$$\frac{d[T_h]}{dt} = \left(\lambda_{T_hD}[D] + \lambda_{T_hM}[M] + \lambda_{T_h\mu_1}[\mu_1]\right)[T_N] - \left(\delta_{T_h\mu_2}[\mu_2] + \delta_{T_hT_r}[T_r] + \delta_{T_h}\right)[T_h] \quad \text{(Equation 6)}$$

$$\frac{d[T_C]}{dt} = \left(\lambda_{T_CT_h}[T_h] + \lambda_{T_CD}[D]\right)[T_N] - \left(\delta_{T_C\mu_2}[\mu_2] + \delta_{T_CT_r}[T_r] + \delta_{T_C}\right)[T_C] \quad \text{(Equation 7)}$$

$$\frac{d[T_r]}{dt} = \left(\lambda_{T_rT_h}[T_h] + \lambda_{T_r\mu_2}[\mu_2] + \lambda_{T_rG_\beta}[G_\beta]\right)[T_N] - \left(\delta_{T_r\mu_1}[\mu_1] + \delta_{T_r}\right)[T_r] \quad \text{(Equation 8)}$$

$$\frac{d[D_N]}{dt} = A_{D_N} - \left(\lambda_{DH}[H] + \lambda_{DC}[C]\right)[D_N] - \left(\delta_{DH}[H] + \delta_D\right)[D_N] \quad \text{(Equation 9)}$$

$$\frac{d[D]}{dt} = \left(\lambda_{DH}[H] + \lambda_{DC}[C]\right)[D_N] - \left(\delta_{DH}[H] + \delta_{DC}[C] + \delta_D\right)[D] \quad \text{(Equation 10)}$$

$$\frac{d[M]}{dt} = \left(\lambda_{M\mu_2}[\mu_2] + \lambda_{MI_\gamma}[I_\gamma] + \lambda_{MT_h}[T_h]\right)(M_0 - [M]) - \delta_M[M] \quad \text{(Equation 11)}$$

$$\frac{d[C]}{dt} = \left(\lambda_C + \lambda_{C\mu_1}[\mu_1]\right)[C]\left(1 - \frac{[C]}{C_0}\right) - \left(\delta_{CG_\beta}[G_\beta] + \delta_{CI_\gamma}[I_\gamma] + \delta_{CT_C}[T_C] + \delta_C\right)[C] \quad \text{(Equation 12)}$$

$$\frac{d[N]}{dt} = \alpha_{NC}\left(\delta_{CG_\beta}[G_\beta] + \delta_{CI_\gamma}[I_\gamma] + \delta_{CT_C}[T_C] + \delta_C\right)[C] - \delta_N[N] \quad \text{(Equation 13)}$$

$$\frac{d[H]}{dt} = \lambda_{HN}[N] + \lambda_{HM}[M] + \lambda_{HT_h}[T_h] + \lambda_{HT_C}[T_C] + \lambda_{HT_r}[T_r] - \delta_H[H] \quad \text{(Equation 14)}$$

$$\frac{d[\mu_1]}{dt} = \lambda_{\mu_1 T_h}[T_h] + \lambda_{\mu_1 M}[M] + \lambda_{\mu_1 D}[D] - \delta_{\mu_1}[\mu_1] \quad \text{(Equation 15)}$$

$$\frac{d[\mu_2]}{dt} = \lambda_{\mu_2 M}[M] + \lambda_{\mu_2 D}[D] + \lambda_{\mu_2 T_r}[T_r] - \delta_{\mu_2}[\mu_2] \quad \text{(Equation 16)}$$

$$\frac{d[I_\gamma]}{dt} = \lambda_{I_\gamma T_h}[T_h] + \lambda_{I_\gamma T_C}[T_C] + \lambda_{I_\gamma M}[M] - \delta_{I_\gamma}[I_\gamma] \quad \text{(Equation 17)}$$

$$\frac{d[G_\beta]}{dt} = \lambda_{G_\beta M}[M] + \lambda_{G_\beta T_r}[T_r] - \delta_{G_\beta}[G_\beta] \quad \text{(Equation 18)}$$

For understanding our parameter naming scheme, see Table 3. This system of ODE has the general form

$$\frac{d[X_i]}{dt} = f_i([\mathbf{X}], \boldsymbol{\theta}) \quad \text{(Equation 19)}$$

where the right hand side $f_i([\mathbf{X}], \boldsymbol{\theta})$ models the interaction network depicted in Figure 1. The vector $\boldsymbol{\theta} = (\theta_1, \ldots, \theta_{63})$ contains all 63 ODE parameters estimated in the paper[28] using steady-state assumptions for each cluster of patients. These model parameters include each cell and molecule's proliferation, activation, inhibition, and decay rates. These rates are either induced by interaction with other cells and molecules or describe intrinsic properties such as natural production or decay. This paper utilizes the published ODE system as the reaction portion of the RDA PDE model.

Macrophages in the model include both pro- and anti-tumor subtypes. Also, the cytotoxic cells are considered to include the effect of both $CD8^+$ and natural killer cells. We assume that all T-cells in the model differentiate from naive T-cells ($T_N$). Still, we omit $T_N$ in Figure 1 since the differentiation happens primarily outside the tumor microenvironment and in the lymphoid system.[70] To avoid too much complexity, we refrain from including nutrient sources or vasculature in the model.

## The PDE model

The PDE system is then formulated as follows:

$$\frac{d[X_i]}{dt} + b_i\nabla\cdot(\mathbf{v}[X_i]) = D_i\Delta[X_i] + f_i([\mathbf{X}], \boldsymbol{\theta}) + S_i(\mathbf{X}), \quad \text{for } i \in \{1, \ldots, 14\} \quad \text{(Equation 20)}$$

where $\mathbf{v}$ is the advection velocity, $D_i$ is the diffusion coefficient, $f_i([\mathbf{X}], \boldsymbol{\theta})$ is the reaction term from Equation 19, and $S_i(\mathbf{X})$ for $i = 2, 3, \ldots, 7$ are the source terms for immune cells

$$S_i(\mathbf{X}) = \begin{cases} 0.5 & \text{if } \|\mathbf{X} - (A_i, B_i)\|_2^2 \le 0.005, \\ 0 & \text{otherwise} \end{cases} \quad \text{(Equation 21)}$$

where $\mathbf{X}$ is the reference domain coordinates and $(A_i, B_i)$ is the location of immune cell sources in the reference domain. We have seven types of parameters in this model: Activation rates, inhibition rates, natural death or decay, independent production rate, fractions, and diffusion coefficients, see Table 3.

We only model the advection of cell types present within the tumor microenvironment. Hence we take

$$b_i = \begin{cases} 0 & \text{if } i = \{1\} \cup \{10, \ldots, 14\}, \\ 1 & \text{otherwise.} \end{cases} \quad \text{(Equation 22)}$$

The indices $i = \{1\} \cup \{10, \ldots, 14\}$ correspond to naive T-cells and the molecules in the model. The diffusion rates are extracted from the literature. For simplicity, we assume that the volume and surface area of all the cell types is approximately the same; thus, we take their diffusion coefficient to be the same. Since naive T-cells mostly activate outside of the microenvironment (in lymph nodes[71,72]), we assume they are not a part of the computational domain, so we do not consider any diffusion coefficient for them. However, dendritic cells go through activation/maturation in response to other cells and cytokines inside the tumor microenvironment.[73,74] So, with no diffusion and no advection (see Equation 22) considered for the naive T-cells, they are the only state variable modeled via an ODE. See Table 2 for the diffusion coefficient values.

Ramos proves the existence and uniqueness of a solution for a PDE system similar to the one introduced in Equation 20 using an iterative method that takes advantage of Banach's fixed point theorem.[75] The PDE system Equation 20 can be coupled with a solid linear elasticity problem. This coupling can help determine the solid tumor's deformation and its cellular constituents' velocity field. To establish the coupling, we use a method applied by several other researchers.[76–78] We start by assuming that the change in cells' volume and surface area is negligible and that the solid tumor is densely packed with no significant gaps or holes inside. So, the sum of cell densities in the tumor microenvironment is a constant, namely $c$, i.e.

$$\sum_{i \in I} [X_i] = c, \quad \text{(Equation 23)}$$

where $I = \{2, 3, 4, 5, 6, 8, 9\}$ contains the indices referring to cell types involved in the tumor microenvironment. Human tissue (in all organs), on average, has the density $1 \frac{g}{cm^3}$,[79] so we take $c = 1$. Thereafter, summing the Equation 20 over $I$ and using the Equation 23, yields:

$$\frac{d}{dt}\left(\sum_{i \in I}[X_i]\right) + b_i \nabla \cdot \left(\mathbf{v} \sum_{i \in I}[X_i]\right) = D_i \Delta \left(\sum_{i \in I}[X_i]\right) + \sum_{i \in I} f_i([\mathbf{X}], \boldsymbol{\theta}) + \sum_{i=2}^{7} S_i(\mathbf{X}). \quad \text{(Equation 24)}$$

But since $\sum_{i \in I}[X_i]$ is constant, its spatial and temporal derivatives are zero. So, Equation 24 simplifies to give

$$\nabla \cdot \mathbf{v} = \frac{\sum_{i \in I} f_i([\mathbf{X}], \boldsymbol{\theta}) + \sum_{i=2}^{7} S_i(\mathbf{X})}{c}, \quad \text{(Equation 25)}$$

which can be rewritten in terms of the displacement $\mathbf{u}$ as:

$$\nabla \cdot \left(\frac{\partial \mathbf{u}}{\partial t}\right) = \frac{\partial}{\partial t}(\nabla \cdot \mathbf{u}) = \frac{\sum_{i \in I} f_i([\mathbf{X}], \boldsymbol{\theta}) + \sum_{i=2}^{7} S_i(\mathbf{X})}{c}. \quad \text{(Equation 26)}$$

Next, we take the incompressible Cauchy stress tensor

$$\boldsymbol{\sigma} = -p\mathbf{I} + \mu\left(\nabla \mathbf{u} + \nabla \mathbf{u}^T\right), \quad \text{(Equation 27)}$$

where $p$ is the hydrostatic pressure, $\mathbf{I}$ is the identity matrix and $\mu$ is the shear modulus. Balance of momentum gives

$$\frac{d\mathbf{v}}{dt} + \nabla \cdot \boldsymbol{\sigma} = \mathbf{B}, \quad \text{(Equation 28)}$$

where $\mathbf{B}$ is the body force. Now, neglecting the body forces and tissue inertia gives us

$$\nabla \cdot \boldsymbol{\sigma} = 0. \quad \text{(Equation 29)}$$

The derivation of the constitutive law Equation 27 and the balance of linear momentum are standard procedures covered in many continuum mechanics books.[80,81] Moreover, we assume that the cell-cell adhesion forces keep the tumor from falling apart.[76,77] So, on the boundary of the tumor, we have

$$\boldsymbol{\sigma}\mathbf{n} = -\kappa\gamma\mathbf{n}, \quad \text{(Equation 30)}$$

where $\mathbf{n}$ and $\kappa$ are the point-wise defined unit outward normal vector and mean curvature for the boundary, respectively, and $\gamma$ is the cell-cell adhesion force. Sancho et al. propose $\gamma = 200 \frac{(mg)\cdot(mm)}{s^2}$ for in-vitro cell--cell'adhesion forces.[82] Also, Deptula et al. report the average Young modulus $E = 7500$ kPa for colon

cancer considering the Poisson ratio $\nu = 0.5$ for all their samples.[83] Using the conversion $\mu = \frac{E}{2(1+\nu)}$ we can take $\mu = 2500$ Pa. However, after scaling the problem by $\mu$ we can take $\widehat{\mu} = 1$ and $\widehat{\gamma} = 0.08$.

Finally, the mechanical problem we have introduced so far has a non-trivial three-dimensional (six if in 3D) kernel $Z$ consisting of the basis vectors of rigid rotation and translation,[84] namely

$$\mathbf{u}_0 = \mathbf{a} + \mathbf{b} \times \mathbf{x}, \quad p_0 = 0 \tag{Equation 31}$$

where $\mathbf{a}$ and $\mathbf{b}$ are arbitrary constant vectors and $\mathbf{x}$ is the Eulerian coordinate vector (i.e., coordinates of the deformed domain). In other words, if the displacement field $\mathbf{u}$ maps the reference domain coordinates to $\mathbf{x}$ and satisfies Equation 29, then any rigid rotation and translation of it also satisfies Equation 29 and gives a rigid rotation and translation of $\mathbf{x}$. This jeopardizes the uniqueness of the solution, given that there are infinitely many translated and rotated versions of each solution. Therefore, To ensure the uniqueness of the solution, we add the following equation to our mechanical problem:

$$l(\mathbf{u}) = \sum_{i=1}^{3} (\mathbf{u}, \mathbf{z}_i)_\Omega \mathbf{z}_i = 0 \tag{Equation 32}$$

where $\mathbf{z}_k$ are basis elements for $Z$ and $(\mathbf{u}, \mathbf{z}_k)_\Omega = \int_\Omega \mathbf{u}(x)\mathbf{z}_k(x)dx$. In other words, if $\mathbf{u}(x)$ is a solution to our mechanical problem and satisfies Equation 32, then it is orthogonal to $Z$. Given $\Omega(t)$ and $\Gamma(t)$ as the domain and its boundary at time $t$, it is customary to add Equation 32 to Equation 29 and rewrite the problem as:

$$\begin{cases} \nabla \cdot \boldsymbol{\sigma} + l(\mathbf{u}) = 0 \ \text{ in } \Omega(t) \\ \dfrac{d}{dt}(\nabla \cdot \mathbf{u}) = \dfrac{\sum_{i \in I} f_i([\mathbf{X}], \boldsymbol{\theta}) + \sum_{i=2}^{7} S_i(\mathbf{x})}{c} \ \text{ in } \Omega(t) \\ \boldsymbol{\sigma}\mathbf{n} = -\kappa\gamma\mathbf{n} \text{ on } \Gamma(t) \end{cases} \tag{Equation 33}$$

The Schmidt lemma[85] guarantees the existence and uniqueness of a solution for problem Equation 33.

## Weak forms and discretization

Let $\widehat{\boldsymbol{\xi}}$ and $q$ be appropriate arbitrary vector and scalar test functions, respectively. Then multiplying both sides of Equation 25 by $q$ and both sides of Equation 29 by $\widehat{\boldsymbol{\xi}}$ and integrating over $\Omega(t)$ gives

$$\int_{\Omega(t)} \frac{d}{dt}(\nabla \cdot \mathbf{u}) q \, dx = \int_{\Omega(t)} \frac{\sum_{i \in I} f_i([\mathbf{X}], \boldsymbol{\theta}) + \sum_{i=2}^{7} S_i(\mathbf{X})}{c} q \, dx \tag{Equation 34}$$

$$\int_{\Omega(t)} (\nabla \cdot \boldsymbol{\sigma}) \cdot \widehat{\boldsymbol{\xi}} \, dx = 0. \tag{Equation 35}$$

Applying integration by parts to Equation 35, we get

$$\int_{\Omega(t)} \boldsymbol{\sigma} : \nabla \widehat{\boldsymbol{\xi}} \, dx - \int_{\Gamma(t)} \boldsymbol{\sigma}\mathbf{n} \cdot \widehat{\boldsymbol{\xi}} \, ds = 0. \tag{Equation 36}$$

Replacing $\boldsymbol{\sigma}\mathbf{n}$ with $-\gamma\kappa\mathbf{n}$ from Equation 30 and summing up Equations 34 and 36 results in the following weak form:

$$\begin{aligned} \mathcal{F}(\mathbf{u}, p, \widehat{\boldsymbol{\xi}}, q) &= \int_{\Omega(t)} \boldsymbol{\sigma} : \nabla \widehat{\boldsymbol{\xi}} \, dx + \int_{\Gamma(t)} \gamma\kappa\mathbf{n} \cdot \widehat{\boldsymbol{\xi}} \, ds \\ &+ \int_{\Omega(t)} \left( \frac{d}{dt}(\nabla \cdot \mathbf{u}) - \frac{\sum_{i \in I} f_i([\mathbf{X}], \boldsymbol{\theta}) + \sum_{i=2}^{7} S_i(\mathbf{X})}{c} \right) q \, dx = 0. \end{aligned} \tag{Equation 37}$$

Then solving the strong forms Equations 29 and 30 corresponds to searching for a pair $(\mathbf{u}, p)$ which satisfies the weak form Equation 37. Similarly, We can turn Equation 32 into a weak constraint using Lagrange multipliers. In other words, instead of finding $\mathbf{u}$ which satisfies the strong Equation 32 we seek Lagrange multiplier vector $\widehat{\boldsymbol{\lambda}} = (\lambda_1, \lambda_2, \lambda_3)$ which satisfy the weak form

$$\mathcal{L}(\mathbf{u},\widehat{\boldsymbol{\lambda}},\widehat{\boldsymbol{\xi}},\widehat{\boldsymbol{\omega}}) = \int_{\Omega(t)}\left[\sum_{i=1}^{3}\lambda_i(\widehat{\boldsymbol{\xi}}\cdot\mathbf{z}_i)\right]dx + \int_{\Omega(t)}\left[\sum_{i=1}^{3}\omega_i(\mathbf{u}\cdot\mathbf{z}_i)\right]dx = 0, \quad \text{(Equation 38)}$$

for all appropriate test vector functions $\widehat{\boldsymbol{\omega}} = (\omega_1,\omega_2,\omega_3)$ and $i = 1,2,3$ (for more details see V.A. Solonnikov (1999)[84]). These $\lambda_i$ s conveniently replace the inner products $(\mathbf{u},\mathbf{z}_i)_\Omega$ in the weak form. Therefore, in the weak sense, problem Equation 33 turns into finding $(\mathbf{u},p,\widehat{\boldsymbol{\lambda}})$ which uniquely satisfies the weak form:

$$\mathcal{F}(\mathbf{u},p,\widehat{\boldsymbol{\xi}},q) + \mathcal{L}(\mathbf{u},\widehat{\boldsymbol{\lambda}},\widehat{\boldsymbol{\xi}},\widehat{\boldsymbol{\omega}}) = 0 \quad \text{(Equation 39)}$$

for all choices of test functions $\widehat{\boldsymbol{\xi}}$,$q$, and $\widehat{\boldsymbol{\omega}}$. We then use $\mathbf{u}$ to displace the domain $\Omega(t)$ and the boundary $\Gamma(t)$ to $\Omega(t+1)$ and $\Gamma(t+1)$ respectively.

For numerical convenience, the RDA system Equation 20 can be written in the Eulerian form:

$$D_t[X_i] + b_i[X_i]\nabla\cdot\mathbf{v} = D_i\Delta[X_i] + f_i([\mathbf{X},\boldsymbol{\theta}) + S_i(\mathbf{x}), \text{for } i\in\{1,\ldots,14\} \quad \text{(Equation 40)}$$

where $D_t = \frac{d}{dt}+\mathbf{v}\cdot\nabla$ is the material derivative and $\mathbf{x}$ is $\mathbf{x} = \mathbf{X}+\mathbf{u}$, namely the current domain coordinates. This makes the numerical methods easier since we always solve this problem in the current/deformed domain. Let's assume that the deformed domain and boundary are $\Omega(t+1)$ and $\Gamma(t+1)$. Using the appropriate test functions $\zeta_i$ for $i = 1,\ldots,14$, we can write the weak form for the system Equation 40:

$$\sum_{i=1}^{14}\left[\int_{\Omega(t+1)}(D_t[X_i] + b_i[X_i]\nabla\cdot\mathbf{v} - f_i([\mathbf{X},\boldsymbol{\theta}) - S_i(\mathbf{x}))\zeta_i\,dx\right] + \sum_{i=1}^{14}\left[\int_{\Omega(t+1)}D_i\Delta[X_i]\cdot\zeta_i\,dx\right] = 0. \quad \text{(Equation 41)}$$

Then using integration by parts on the second integral, we obtain:

$$\mathcal{B}([X_i],\zeta_i,D_t[X_i]) = \sum_{i=1}^{14}\left[\int_{\Omega(t+1)}(D_t[X_i] + b_i[X_i]\nabla\cdot\mathbf{v} - f_i([\mathbf{X},\boldsymbol{\theta}) - S_i(\mathbf{x}))\zeta_i\,dx\right] + \sum_{i=1}^{14}\left[\int_{\Omega(t+1)}D_i(\nabla[X_i]\cdot\nabla\zeta_i)\,dx\right] = 0. \quad \text{(Equation 42)}$$

For the discretization, we consider $\Omega_h^t$ to be a triangulated discrete mesh approximating $\Omega(t)$. Let $\mathcal{V}_h^t$ and $\mathcal{S}_h^t$ be piece-wise quartic vector function space and piece-wise linear scalar function space defined on $\Omega_h^t$, respectively. We use a mixed finite element space $\mathcal{W}_h^t$ for our solution space:

$$\mathcal{W}_h^t = \left\{(\mathbf{u}_h^t,p_h^t,\widehat{\boldsymbol{\lambda}})\,|\,\mathbf{u}_h^t\in\mathcal{V}_h^t, p_h^t\in\mathcal{S}_h^t,\widehat{\boldsymbol{\lambda}}\in\mathbb{R}^3\right\}. \quad \text{(Equation 43)}$$

Notice that we do not use any discretization for $\mathbb{R}^3$. That's because $\widehat{\boldsymbol{\lambda}}$ is a constant vector containing Lagrange multipliers. If we denote the set of basis functions for $\mathcal{V}_h^t$ and $\mathcal{S}_h^t$ by $\{\widehat{\boldsymbol{\xi}}_{h,i}^t\}_{i=1}^N$ and $\{q_{h,i}^t\}_{i=1}^M$, then:

$$\mathbf{u}_h^t = \sum_{i=1}^{N}c_i^t\widehat{\boldsymbol{\xi}}_{h,i}^t, \quad p_h^t = \sum_{i=1}^{M}k_i^t q_{h,i}^t. \quad \text{(Equation 44)}$$

So the discretized version of problem Equation 39 reduces to finding the solution $(\mathbf{u}_h^t,p_h^t,\widehat{\boldsymbol{\lambda}})$ for

$$\mathcal{F}_h\left(\mathbf{u}_h^t,p_h^t,\widehat{\boldsymbol{\xi}}_{h,i}^t,q_{h,i}^t\right) + \mathcal{L}_h\left(\mathbf{u}_h^t,\widehat{\boldsymbol{\lambda}},\widehat{\boldsymbol{\xi}}_{h,i}^t,\widehat{\boldsymbol{\omega}}\right) = 0, \quad \text{(Equation 45)}$$

for all basis functions $\widehat{\boldsymbol{\xi}}_{h,i}^t\in\mathcal{V}_h^t$, $q_{h,i}^t\in\mathcal{S}_h^t$ and $\widehat{\boldsymbol{\omega}}\in\mathbb{R}^3$. Here, we spared the details about the numerical integration and differentiation distinguishing the operators $\mathcal{F}_h$ and $\mathcal{L}_h$ from $\mathcal{F}$ and $\mathcal{L}$, as well as the replacement of test functions with basis functions. An avid reader can refer to any basic finite element book for more information (e.g., see chapter 5 of the book by Gander and Kwok for a quick introduction[86]).

After retrieving $\mathbf{u}_h^t$, we displace the mesh $\Omega_h^t$ to $\Omega_h^{t+1}$. So, the flow map $x(x_h^0,t+1) = x(x_h^0,t)+\mathbf{u}_h^t$ is applied for moving from $\Omega_h^t$ to $\Omega_h^{t+1}$. The material derivative can be discretized in $\Omega_h^{t+1}$ using a forward Euler scheme:

$$D_t[X_i]\approx D_{h,t}[X_i] := \frac{[X_i]\left(x\left(x_h^0,t+1\right),t+1\right) - [X_i]\left(x\left(x_h^0,t\right),t\right)}{dt}, \quad \text{(Equation 46)}$$

where $dt$ is a small enough time step. Here, we do not need to interpolate anything since we are solving the problem in $\Omega_h^{t+1}$, and the mesh points move with the flow map. Furthermore, the discrete velocity field $\mathbf{v}_h^t$ can be calculated by:

$$\mathbf{v}_h^t \approx \frac{\mathbf{u}_h^t}{dt}. \quad \text{(Equation 47)}$$

Again, since the mesh points move with the flow map.

Looking back at Table 2, we can see that the cell diffusion coefficient is very small. This may lead to an advection or reaction-dominated numerical problem, resulting in numerical instabilities. To circumvent this issue, we use a space enrichment method using bubble elements.[87–89] This method is a very efficient stabilization method since it does not increase the size of the problem significantly. For the moved mesh $\Omega_h^{t+1}$ we define bubble-enriched piece-wise linear function spaces $\mathcal{Q}_{h,B}^{t+1} = \mathcal{Q}_h^{t+1} \oplus \mathcal{Q}_B^{t+1}$, and use the mixed space given by

$$\mathcal{E}_h^{t+1} = \left\{ \left( [X_1]_h^{t+1}, \ldots, [X_{14}]_h^{t+1} \right) \middle| [X_i]_h^{t+1} \in \mathcal{Q}_{h,B}^{t+1} \right\}. \quad \text{(Equation 48)}$$

Finally, we solve

$$\mathcal{B}_h\left( [X_i]_h^{t+1}, \zeta_{h,i}^{t+1}, D_{h,t}[X_i]_h^{t+1} \right) = 0, \quad \text{for all basis functions } \zeta_{h,i}^{t+1} \text{ in } \mathcal{E}_h^{t+1} \quad \text{(Equation 49)}$$

for cells and molecules concentrations in the current domain.

## Simulation

We use FEniCS for the numerical simulation of our problem.[68] FEniCS is a powerful Python package that makes finite-element-based computations very easy. Complicated constructions such as higher-dimensional spaces, mixed spaces, and element-based enrichment are done in just a few lines. We also used GMSH software, which can easily handle structured and unstructured meshes and has several meshing algorithms, to create the domain surface and boundary meshes[69] as creating meshes with several sub-domains and interfaces can be done painlessly through GMSH. The bonus feature of the mentioned packages is that they can communicate with each other dynamically. We call GMSH through FEniCS for faster and more flexible re-meshing.

## Adjoint-based sensitivity analysis

We performed Adjoint-based Sensitivity Analysis (ABSA).[90] Suppose we have a general system consisting of $N$ number of PDEs

$$\mathbf{F}(\mathbf{x}, \boldsymbol{\theta}) = 0 \quad \text{(Equation 50)}$$

where the solution $\mathbf{x}$ can be considered an implicit function of the parameters $\boldsymbol{\theta}$. Suppose we have a quantity of interest $J(\mathbf{x})$, and we are interested to know its sensitivity to the parameters, i.e., $\frac{\partial J}{\partial \boldsymbol{\theta}}$. The direct way to do so is to perturb the parameters and see how they affect the quantity of interest. This method is not generally a bad approach, especially if $\boldsymbol{\theta}$ is low-dimensional. However, it can quickly become impossible computationally if $\boldsymbol{\theta}$ is a high-dimensional vector. Moreover, if the Equation 50 is time-dependent, it can significantly add to the computational burden, and our problem is a time and space-dependent PDE system with 82 parameters. A way to circumvent this issue is to use ABSA. The idea of this method is to obviate the dependence of $\frac{\partial J}{\partial \boldsymbol{\theta}}$ on the solution $\mathbf{x}$ as much as possible. From Equation 50, we can immediately deduce that

$$J(\mathbf{x}) = J(\mathbf{x}) + \mathbf{F}(\mathbf{x}, \boldsymbol{\theta}), \quad \text{(Equation 51)}$$

or more generally,

$$J(\mathbf{x}) = J(\mathbf{x}) + \psi^T \mathbf{F}(\mathbf{x}, \boldsymbol{\theta}), \quad \text{(Equation 52)}$$

holds for all vectors $\psi \in \mathbb{R}^N$. Now, if we slightly perturb $\boldsymbol{\theta}$, it will cause a slight perturbation in $\mathbf{x}$ and $J$, i.e.:

$$\delta\boldsymbol{\theta} \rightarrow \delta\mathbf{x} \rightarrow \delta J. \quad \text{(Equation 53)}$$

By the way of the chain rule, this can be rewritten using Equation 52 as:

$$\delta J = \frac{\partial J}{\partial \mathbf{x}}\delta \mathbf{x} + \psi^T\left(\frac{\partial \mathbf{F}}{\partial \mathbf{x}}\delta \mathbf{x} + \frac{\partial \mathbf{F}}{\partial \boldsymbol{\theta}}\delta \boldsymbol{\theta}\right) = \underbrace{\left(\frac{\partial J}{\partial \mathbf{x}} + \psi^T\frac{\partial \mathbf{F}}{\partial \mathbf{x}}\right)}_{(*)}\delta \mathbf{x} + \psi^T\frac{\partial \mathbf{F}}{\partial \boldsymbol{\theta}}\delta \boldsymbol{\theta}. \quad \text{(Equation 54)}$$

So if we set (*) equal to zero, we have achieved our goal. In fact, the equation

$$\left(\frac{\partial \mathbf{F}}{\partial \mathbf{x}}\right)^T \boldsymbol{\psi} = -\left(\frac{\partial J}{\partial \mathbf{x}}\right)^T \quad \text{(Equation 55)}$$

is known as the adjoint equation. Since $\frac{\partial \mathbf{F}}{\partial \mathbf{x}}$ is non-singular by the implicit function theorem, it is guaranteed to give us a vector $\boldsymbol{\psi}$ which makes (*) from the Equation 54 zero. Therefore, using the solution $\boldsymbol{\psi}$ from Equation 55 we can rewrite Equation 54 completely independent of $\mathbf{x}$ as follows:

$$\frac{\partial J}{\partial \boldsymbol{\theta}} = \boldsymbol{\psi}^T\frac{\partial \mathbf{F}}{\partial \boldsymbol{\theta}}. \quad \text{(Equation 56)}$$

Note that we still need to calculate $\mathbf{x}$ for a nominal set of parameters $\boldsymbol{\theta}$ from Equation 50 to be able to get $\boldsymbol{\psi}$ from the adjoint equation. But, this needs to be done only once, and after that, the sensitivity calculation is independent of the solution. Computationally, we utilized a FEniCS package called `dolfin-adjoint`, which makes these calculations much easier.[91]

## QUANTIFICATION AND STATISTICAL ANALYSIS

The detail of the statistical analysis of data for kinetic parameter estimations can be found in the paper by Kirshtein et al.[28]

The half-concentration values refer to values that are exactly between the minimum and maximum values. The half-concentration contours in Figures 5, 9, 12, and S1–S3 mark the points in the region which have half-concentration values. Therefore, they separate the regions with values higher than the half-concentration values from the regions with values lower. Using the `Contours` command in Paraview (5.10.0, Kitware, Inc.) we can determine these contours for a concentration field.

Moreover, the maximum, minimum, and mean curves in Figures 3 and 4 refer to the maximum, minimum and mean density/concentration of their associated variable across the whole domain at time $t = 3000$ days. Using the `Descriptive Statistics` filter in Paraview (5.10.0, Kitware, Inc.) we can extract these measurements and then using `Plot selection over time` command, we can plot them.